Evolutionary growth of molecular clouds as traced by their infrared bright fraction

E. J. Watkins [1,2]★ N. Peretto [3] A. J. Rigby [4] R. J. Smith [5] K. Kreckel [2] and G. A. Fuller[1,6]

[1]*Jodrell Bank Centre for Astrophysics, Department of Physics and Astronomy, University of Manchester, Oxford Road, Manchester M13 9PL, UK*
[2]*Astronomisches Rechen-Institut, Zentrum für Astronomie der Universität at Heidelberg, Mönchhofstraße 12-14, D-69120 Heidelberg, Germany*
[3]*Cardiff Hub for Astrophysics Research & Technology, School of Physics & Astronomy, Cardiff University, Queens Buildings, The Parade, Cardiff CF24 3AA, UK*
[4]*School of Physics and Astronomy, University of Leeds, Leeds LS2 9JT, UK*
[5]*School of Physics and Astronomy, University of St Andrews, North Haugh, St Andrews KY16 9SS, UK*
[6]*I. Physikalisches Institut, University of Cologne, Zülpicher Str. 77, D-50937 Köln, Germany*

ABSTRACT

Understanding how stars form, evolve, and impact molecular clouds is key to understanding why star formation is such an inefficient process globally. In this paper, we use the infrared bright fraction, f_{IRB} (the fraction of a given molecular cloud that appears bright against the 8 μm Milky Way background) as a proxy for time evolution to test how cloud properties change as star formation evolves. We apply this metric to 12 000 high-mass star-forming molecular clouds we identify using the *Herschel*–Hi-GAL survey between $|\ell| < 70°$ on the Milky Way plane. We find clouds are not static while forming stars. Instead, molecular clouds continuously gain mass while star formation progresses. By performing principal component analysis on the cloud properties, we find that they evolve down two paths distinguished by their mass gain. Most clouds (80 per cent) gain four times more mass as a function of f_{IRB}. The remaining 20 per cent experience an extreme period of growth, growing in mass by a factor of 150 on average and during this period, they initially gain mass fast enough to outpace their star formation. For all clouds, it is only after half their area becomes star forming that mass-loss occurs. We expect stellar feedback and potentially galactic shear is responsible. By analysing cloud positions, we suggest that the rate of mass growth may be linked to the larger galactic environment. Altogether, these results have strong implications on how we assess star-forming ability on cloud scales when assuming molecular cloud masses are fixed in time.

Key words: stars: formation – ISM: clouds – infrared: ISM.

1 INTRODUCTION

Stars form in the small fraction of the interstellar stellar medium (ISM) that contains dense (>1000 cm^{-3}) inhomogeneous molecular structures. On galactic scales, large-scale dynamic motions and stellar feedback organize these structures into spiral arms, large galactic filaments, and voids (Elmegreen 2011; Ragan et al. 2014; Zucker, Battersby & Goodman 2015; Grisdale et al. 2017; Watkins et al. 2023). On smaller scales (∼10 pc), the added influence of self-gravity and turbulence (Chen et al. 2020; Abe et al. 2021) organizes the gas into filamentary molecular clouds (Schneider & Elmegreen 1979; Molinari et al. 2010b) and hubs (Myers 2009; Anderson et al. 2021) that can contain star-forming clumps (∼0.1–1 pc) and cores (< 0.1 pc).

While the exact definition and nature of a molecular cloud varies depending on the spatial scale resolved and the tracer used, they typically represent where we expect molecular gas can evolve into discrete star forming complexes (Chevance et al. 2020a). Stellar

feedback from these complexes, and shear from larger scales disrupts molecular gas across these scales. In particular, it has been shown that stellar feedback is necessary to explain low star formation efficiencies (SFEs) in the nearby Universe (Krumholz, Klein & McKee 2007; Hopkins et al. 2014). Therefore, a complete theory of star formation in molecular gas structures needs a unified picture of star formation on large and small scales (Dobbs, Pringle & Duarte-Cabral 2015; Pettitt et al. 2020; Smith et al. 2020). However, because molecular clouds evolve over millions of years, we cannot follow its exact evolution observationally for individual structures. We must instead piece it together statistically using a large sample of molecular clouds in different environments at different evolutionary stages. These samples allow us to estimate the timeline for a given molecular cloud by using the average properties of less and more evolved clouds as surrogates, providing we have a tracer that is able to detect the presence or absence of star formation. Such techniques have been employed in various forms in the Milky Way and nearby galaxies (Battersby, Bally & Svoboda 2017; Chevance et al. 2020b; Mazumdar et al. 2021; Rigby et al. 2021, 2024). For example Battersby et al. (2017) used 8 μm emission to trace both the amount of gas that is currently starless or is star forming on a pixel-by-pixel basis. This

allowed them to measure the fraction of high-mass pixels (as defined using Hi-GAL data) that were infrared bright or dark over $2° × 2°$ of the Milky Way plane. They found that ∼65 per cent of pixels were quiescent while ∼ 35 per cent star forming, and when linked to co-spatial objects with known lifetimes, they estimated the starless and star-forming phases of high-mass pixels were 0.2–1.7 and 0.1–0.7 Myr, respectively.

Observations at 8 μm are somewhat unique in how it traces the presence or absence of star formation in the Milky Way. The diffuse background ∼8 μm emission across the inner $\ell < |70°|$ part of the Milky Way plane (with typical values of the order ∼100 MJy sr^{-1}) is bright enough that it can be absorbed by foreground cold dust, appearing as dark patches against the bright emission (Peretto & Fuller 2009). Cold dust traces quiescent starless molecular gas; therefore, it can be used to trace absent star formation. At the same time, direct emission from protostellar objects is sufficiently bright to outshine the diffuse background in this band. Moreover, the stellar light [especially ultraviolet (UV) light] emitted by recently formed high-mass stars cause polycyclic aromatic hydrocarbons (PAHs) to fluoresce throughout the mid-infrared (mid-IR). This is particularly bright at ∼8 μm, as it covers multiple PAHs bands, while the stellar and cold dust continuum over this range are simultaneously low (Marble et al. 2010). Statistically, feedback from high-mass stars, which UV photons trace, marks the end of the star formation in molecular gas (Chevance et al. 2020b), and so it can also be used to trace the progression of star formation. Therefore, we can use broad-band 8 μm observations to calculate a relative evolutionary timeline and status of the star formation within molecular clouds on a cloud-by-cloud basis across the Milky Way plane.

For this purpose, we structure the paper as follows. Section 2 introduces the data sets needed to identify molecular clouds and to determine their evolutionary stage and properties. In Section 3, we produce a catalogue of molecular clouds across the Milky Way plane. Section 4 outlines how to estimate how evolved the star formation is in molecular clouds using mid-IR emission and tests how effective it is as an evolutionary tracer. In Section 5, we present our results and trends of cloud properties as a function of evolutionary stage. In Section 6, we discuss the implications of these results in the context of cloud evolution and present our closing remarks in Section 7.

2 OBSERVATIONS AND SURVEY CATALOGUES

2.1 Hi-GAL survey and source catalogues

The *Herschel* infrared Galactic Plane Survey (Hi-GAL) was a key project of *Herschel* (Molinari et al. 2010a) to measure cold dust as a tracer of molecular gas and star formation. It mapped ∼ 1° above and below the Galactic plane over a 360° view at 70, 160, 250, 350, and 500 μm with resolutions of 7, 12, 18, 24, and 36 arcsec, respectively. In addition to providing individual ∼2.2 deg^2 maps of the Milky Way plane, the Hi-GAL team has produced a compact source catalogue for each waveband, each containing ∼100 000 entries (Molinari et al. 2016). Each catalogue currently covers $|\ell| \lesssim 70°$ and $|b| \le 1°$. Sources were extracted using the CuTEx algorithm (Molinari et al. 2011), which is able to detect sources over a large range of background conditions (both low and high background values).

2.2 GLIMPSE I/II

The Galactic Legacy Infrared Mid-Plane Survey Extraordinaire (GLIMPSE; Churchwell et al. 2009) was a near-to-mid infrared Galactic plane survey taken with the InfraRed Array Camera (IRAC) on-board the *Spitzer Space Telescope* (Fazio et al. 2004; Werner et al. 2004). The survey covered Galactic longitudes of $|\ell| \le 65°$ and Galactic latitudes $|b| \le 1°$ (extending to 1.5° between $|\ell| = 5–2°$ and extending to 2° for longitudes $|\ell| \le 2°$). The survey imaged the sky in 3.6, 4.5, 5.8, and 8.0 μm. 8.0 μm traces both internal heating from protostellar objects and traces H II regions via the fluorescence of PAHs, caused by UV emission. The angular resolution, pixel resolution, and the average rms uncertainty are 1.9 arcsec, 1.2 arcsec, and 0.3 MJy sr^{-1}, respectively, at 8.0 μm for this survey. For this study, we use the 8.0 μm flux density to indicate how much of a given cloud is currently forming stars.

3 MOLECULAR CLOUD CATALOGUE AND PROPERTIES

3.1 Cloud identification

To trace molecular gas, we use dust emission from the Hi-GAL survey between $|\ell| \le 70°|b| \le 1°$. We chose these extents to match the survey extent of GLIMPSE, which we use to trace how evolved the star formation is in Section 4. For Hi-GAL data, we are limited to a 2D projected view, which makes foreground and background emission indistinguishable. As a result, the amount of molecular gas we measure will be overestimated, and the structures we detect will be more extended due to the increased column of gas along the line of sight. To limit these impacts, we use the 18″ resolution background subtracted H$_2$ column density maps derived from Hi-GAL observations from Peretto et al. (2016). The background has been defined using a median filter that is 10′ in size (matching the largest *Spitzer* dark clouds found in the GLIMPSE survey), which removes extended emission on scales larger than 10′. This also sets the maximum size scale of molecular structures that we identify. In general, molecular clouds are nebulously defined objects due to the multiscalar and continuous nature of the ISM. As a result, their appearance is not only dependent on the tracer used, but also the spatial scales being probed. Multiple detection approaches (which lead to different structures being identified as molecular clouds) are therefore needed and have been developed to detect molecular clouds (Williams, de Geus & Blitz 1994; Rosolowsky & Leroy 2006; Rosolowsky et al. 2008; Berry 2015; Colombo et al. 2015; Rani et al. 2023).

To minimize the impact of different density thresholds have on structures, we identify clouds using any closed contour above a single column density threshold. For this threshold, we use $1 × 10^{22}$ cm^{-2}. While $1 × 10^{22}$ cm^{-2} might be considered arbitrary and high – especially considering that gas is expected to be molecular and star forming an order of magnitude below this value (Clark & Glover 2014) – it allows us to focus on objects that are close to or beyond the predicted column density threshold needed star formation (Johnstone, Francesco & Kirk 2004; André et al. 2014; Priestley et al. 2023). Finally, a high column density threshold assists with the evolution tracer, discussed further in Section 4.2.

The main disadvantage of a high column density threshold is the artificial segmentation of spatially (and velocity) coherent molecular clouds into smaller substructures (analogous to molecular 'clumps'). Indeed, any column density cut-off results in arbitrary cloud boundaries within a spatially coherent structure at some larger scale due the multiscalar and continuous nature of the ISM. However, by using median-filter-subtracted column density maps, we have already introduced a segmentation scale that limits the maximum size structures can be. Since this size scale is based on GLIMPSE
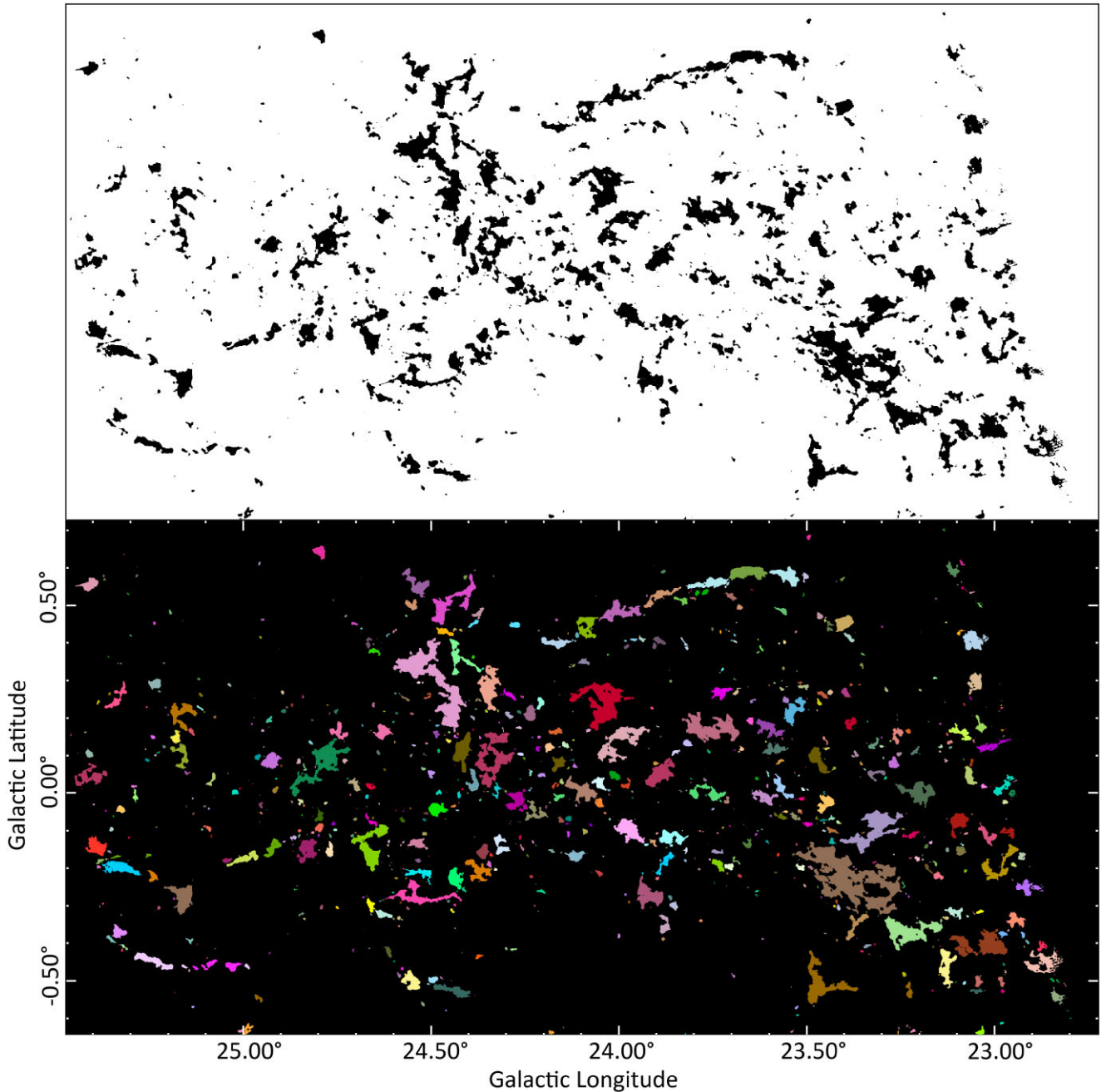
Figure 1. Molecular structures identified in *Herschel* column density data between a galactic longitude of 23 and 25.5°. *Top* panel shows all pixels $\geq 1 \times 10^{22}$ cm^{-2} (solid black colour), where each pixel is 4.5 arcsec in size. *Bottom* panel shows the regions that are identified. Colours indicates the IDs of clouds.

observations, we prioritize studying objects closer to this spatial scale. To do this without lowering the column density threshold, we perform a watershed-like algorithm to connect spatially coherent substructures. Substructures are connected together by generating a binary map equal to 1 for pixels above a column density threshold of 1×10^{22} cm^{-2} and dilating these masks outward by convolving the map with a small Gaussian kernel (see e.g. the top panel of Fig. 1). Any substructures that now touch are considered to be one structure, as indicated on Fig. 2. To avoid structures that span size scales significantly $> 10'$, we only convolve the masks to $21''$. Finally, any structures with an effective area smaller than the resolution of the column density map ($18''$) are removed.

After visual inspection, we find it was able to join most of the gas in known star forming regions (e.g. NGC6334, see Figs 3 and A1), without resulting in degree-sized overmerged structures everywhere, even towards crowded locations closer to the galactic centre. However due to the high column densities found specifically between $|\ell| < 2.5°$, our algorithm always created overmerged objects (see Fig. A2) with extremely large spatial extents ($> 1°$). As a result, we exclude all structures between $|\ell| < 2.5°$ from further analysis.

Before merging we identify 22 851 structures and after we identify 16 343. Of these, 553 are outside the exact GLIMPSE survey area so after removing these, we are left with 15 790. For the rest of this
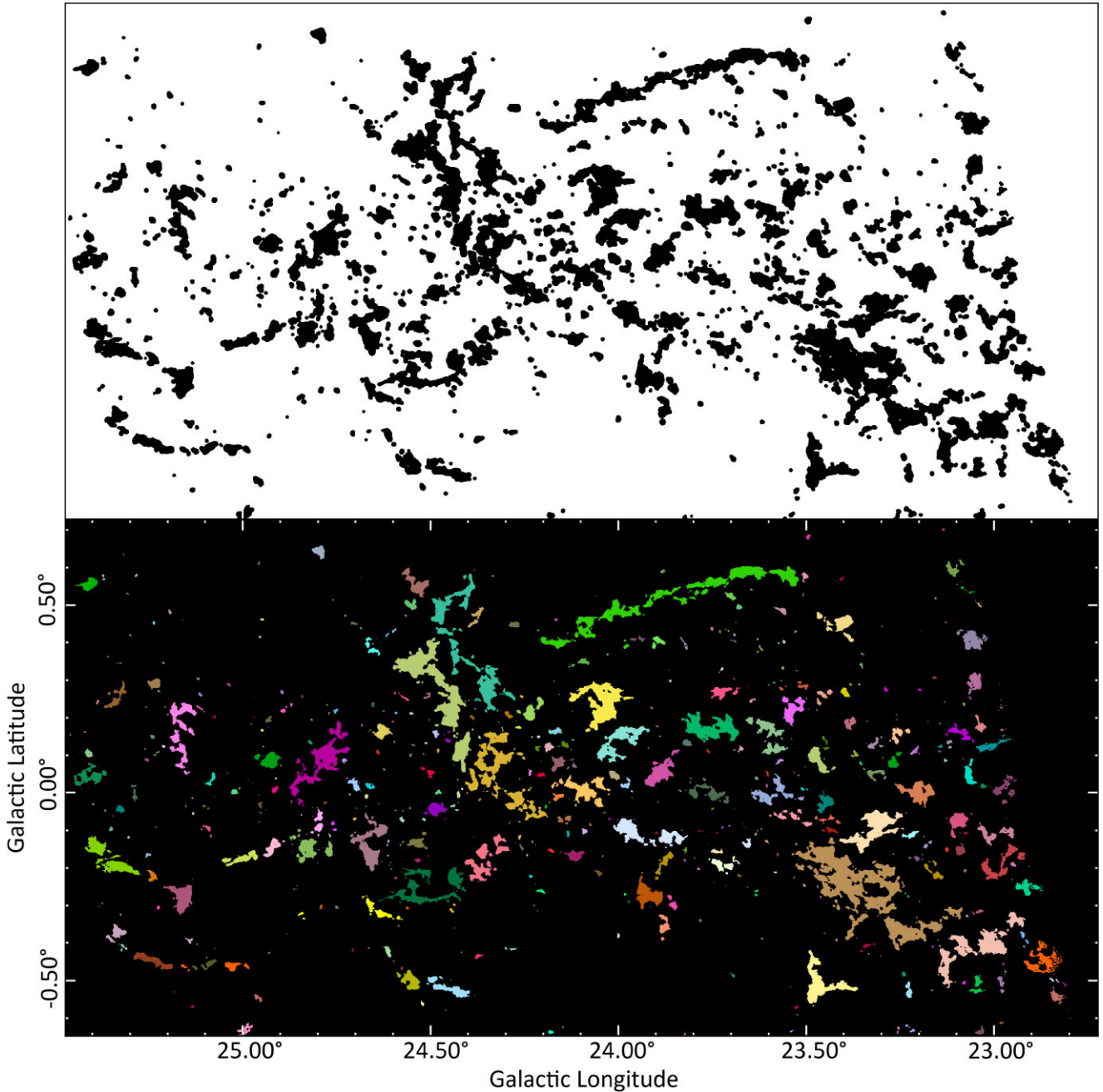
Figure 2. Applying watershed-like algorithm to connect spatial coherent substructures in Fig. 1. *Top* panel illustrates how substructures are connected by convolving the masked data to 21 arcsec. *Bottom* panel shows the large-scale structures identified after the watershed-like algorithm. The colours indicates the ID's of each cloud. See Fig. 1 to compare how substructures have been grouped together.

paper, to simplify discussions, we refer to these grouped structures as molecular clouds (or clouds for short).

3.2 Assigning distances to molecular clouds

The Hi-GAL team calculated the distance catalogue to >150 000 Hi-GAL sources (Mège et al. 2021). These distances were assigned by cross-examining all available distance tracers for each object. If maser parallax measurements were available, the source distance could be determined with a high degree of accuracy. However, only 93 sources in their catalogue had maser parallax measurements.

Therefore, the majority of distances in Mège et al. (2021) were assigned using radial-velocity measurements from molecular line or from H I surveys with a Galactic rotation model. To resolve the near-far kinematic distance ambiguity for each source, the distance was compared to dust extinction, H I absorption features and its projected scale height when these options are available. For example, if a source was seen in absorption, or its distance from the mid-plane at the far distance was significantly greater than the scale height of the Milky Way, then it was unlikely to be at the far distance and so it was assigned the near distance value.
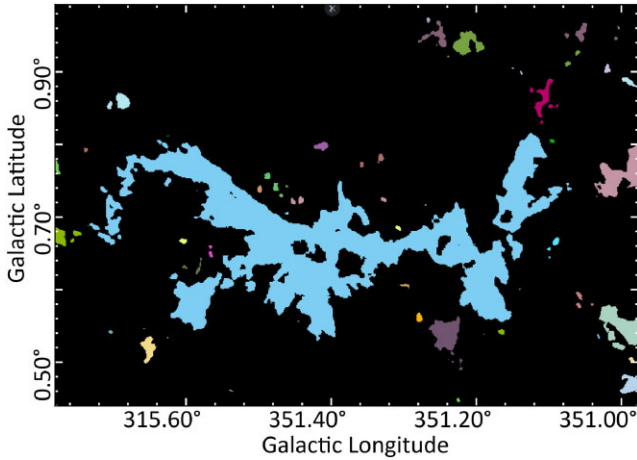
Figure 3. NGC6334 after connecting masks using watershed-like method. Light blue mask in the centre of the image shows NGC6334 where the majority of unconnected masks are merged (and so appear light blue) after performing a watershed-like method. Masks that are not light blue represent independent molecular structures identified in Section 3.1.

Using the Hi-GAL distance catalogue, we assign a distance to each cloud only if their area masked in the previous section directly overlaps with the compact Hi-GAL source. However, complications arise for clouds (and even the initial pre-merged sources) that contain multiple Hi-GAL sources. We find the distance (and velocity) values between sources can disagree due to measurement uncertainties, source crowding along the line of sight or in some instances, clouds contain sources with identical velocities, but their distances are near-far confused. To assign a single distance to a cloud while accounting for these complex situations, we create a decision tree. In summary, the decision tree determines distances and velocities for clouds while eliminating small outliers, and rejecting clouds from further analysis when most of the distances and velocities are dissimilar. Removing such clouds is necessary to account for the fact we only used 2D spatial information when identifying clouds.

The first part of the decision tree passes clouds that contain only a single source and assigns that distance to the cloud. The next part of the decision tree deals with clouds that contain three or more distance values and aims to remove clouds that are unlikely to be spatially coherent in 3D space. For these clouds, we only assign the median distance (and velocity) if >50 per cent of the distances and the velocities remain after sigma clipping (we use the median absolute deviation with a 3σ confidence level); otherwise, we re-perform the sigma clip using the near distances only. If >50 per cent of the distances now remain, we assign the median near-distance value, while the rest do not get a distance assigned and are removed from our sample. We prioritize the near distance since most clouds (70–80 per cent) are located at the near distance (Urquhart et al. 2018). We investigate the impact this decision might have for our results in Appendix B.

The next part of the decision tree deals with clouds where sigma clipping cannot be used. For very coherent distance and velocity values, sigma clipping causes erroneous source rejection and therefore cloud rejection when in fact, the distances of the sources are nearly identical. Therefore, when all the velocities and distances are within ≤2.5 km s^{-1} and ≤0.1 kpc of each other, the median distance is assigned without performing sigma clipping. We chose these limits by inspecting the velocity and distance values present when sigma clipping failed. Increasing these ranges did not significantly increase

the number of clouds accepted; the values are similar enough that sigma clipping failed. However when larger limits are used, the distance and velocity assigned are more likely to be inconsistent with commonly used values found in the literature for known objects.

Finally, if a cloud contains only two distance values, sigma clipping cannot be used. For these clouds, the mean distance is assigned if both the velocities and distances are within ≤5 km s^{-1} and ≤0.2 kpc of each other. Otherwise, no distance is assigned and the cloud is removed. These limits are chosen to match the strict limits we set for coherent clouds (i.e. both clouds can different by ≤2.5 km s^{-1} and ≤0.1 kpc each, which doubles these values). Altogether, we are able to assign distances to 12 686 clouds (75 per cent of the catalogue). We note that 20 of these clouds had distances >30 kpc. These clouds are also rejected, leaving 12 666 clouds, which is comparable to the number of objects identified in Peretto et al. (2016). We are therefore confident we are probing similar spatial scales as this paper.

4 INFRARED BRIGHT FRACTION AS AN EVOLUTIONARY TRACER OF MOLECULAR CLOUDS

On the Milky Way plane, 8 μm emission is able to trace both the presence and absence of star formation within individual clouds when contrasted against the bright background emission. As a result, the fraction of bright emission within the area of a cloud indicates how evolved the star formation is within that clouds. Using this fact, we define a quantity we call the infrared bright fraction (f_{IRB}) to represent this evolution as a fraction between zero and one. For each cloud, f_{IRB} denotes the number of bright pixels over the total number of pixels within a cloud. An f_{IRB} of 0, therefore, represents the earliest stage of star formation (i.e. starless clouds) and 1 indicates star formation is underway in the entire cloud. With this definition, f_{IRB} increase as time increases. The f_{IRB} includes emission from protostellar heating, and PAHs heated by high-mass stars, both of which indicate the star formation is more evolved in the molecular gas.

To calculate f_{IRB}, we subtract the background emission from the GLIMPSE 8 μm maps, leaving a map containing positive (bright) and negative (dark) pixel values. To model the Galactic plane background while accounting for its complex, highly varying emission (i.e. decreasing emission as a function of Galactic latitude and longitude, and local variations due to galactic structures) we use a median filter of size 4.8 arcmin for the entire GLIMPSE survey. After subtraction, we label all positive pixels above the survey RMS (0.3 MJy sr^{-1}) as infrared bright with a value of one and all negative pixels below the survey RMS as infrared dark with a value of zero. Any pixels falling within the RMS noise limit remain unassigned since the pixel value could be caused by noise fluctuations. Very few pixels are left unassigned. We chose 4.8 arcmin to match the average size of the structures we identify in Section 3.1 and because it is similar to the average sizes identified in Peretto & Fuller (2009).

These background-subtracted infrared bright-dark maps have already been successfully applied to clumps found using New IRAM KIDs Array 2 (NIKA2) camera in Rigby et al. (2021) and clumps examined with NOEMA and ALMA in Rigby et al. (2024) to calculate their f_{IRB}. In Fig. 4, we illustrate the background-subtracted infrared bright-dark map between $l = 23°$–$25.5°$, matching the area mapped in Rigby et al. (2021). On the figure, we zoom into a small section that contains a strongly varying background and a cloud that we have identified to check how the map is impacted. Despite the complex background emission, the cloud still appears dark with
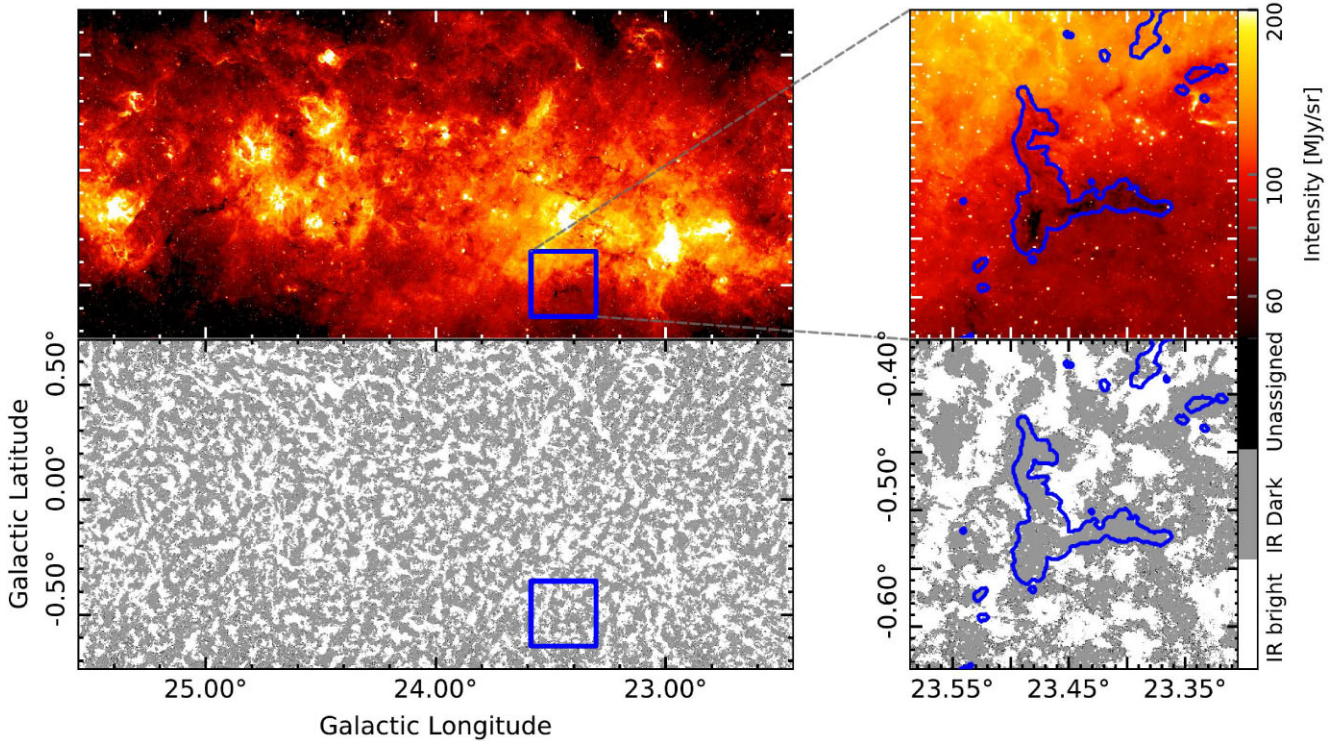
Figure 4. *Spitzer* 8 μm data and its infrared bright map derived by subtracting its background emission, along with its application to molecular clouds. *Top left*: *Spitzer* 8 μm map from the galactic plane (23°–25.5°) showing both bright star forming, and dark quiescent molecular gas. Blue box marks the location showing an example molecular cloud with complex background emission. *Top right*: Example molecular cloud seen in absorption at 8 μm with complex background emission. Blue contour shows the *Hershel* cloud masks above a column density threshold of 1×10^{22} cm^{-2}. *Bottom left*: Infrared bright map after applying a median filter of 4.8′ on the GLIMPSE 8 μm map and subtracting the result away from the original image. Positive pixels are deemed infrared bright (white), negative pixels are deemed infrared dark (grey) and any pixels that fall under the RMS noise (0.3 MJy sr^{-1}) are left unassigned (black). *Bottom right*: Same example region as *top right* but with the infrared bright map shown instead.

a f_{IRB} equal to 0.05, demonstrating our median filter produces an accurate background model.

4.1 Verifying f_{IRB} as a tracer of evolutionary stage

As molecular clouds convert a higher fraction of gas into stars, their instantaneous SFE increases along with their dust temperature. Therefore, we use instantaneous SFEs and dust temperatures to test how well f_{IRB} traces evolution by checking if all three quantities correlate with each other. To measure dust temperatures, we use *Herschel* dust temperatures from Peretto et al. (2016). Since the SFE cannot be measured directly as we do not know the exact amount of stars that have formed, we use 70 μm emission within the cloud (or more specifically, the total 70 μm luminosity of Hi-GAL 70 μm compact sources) as a tracer of the stellar mass and divide it by the mass of the cloud instead. 70 μm emission can be used this way due to a chain of results that link the two properties. In summary, the bolometric luminosity of a protostar approximately equals (i.e. is dominated by) its accretion luminosity and its accretion luminosity is proportional to its protostellar mass (Evans II et al. 2009). Since we do not know its accretion luminosity, we substitute it with its 70 μm luminosity, which was found to be the most reasonable proxy for the accretion luminosity throughout the majority of protostellar evolution (Dunham et al. 2008; Ragan et al. 2012).

In Fig. 5, we plot the total 70 μm luminosity of Hi-GAL sources over cloud mass against average dust temperature for each cloud and colour the markers by its f_{IRB} value. The marker size also represents
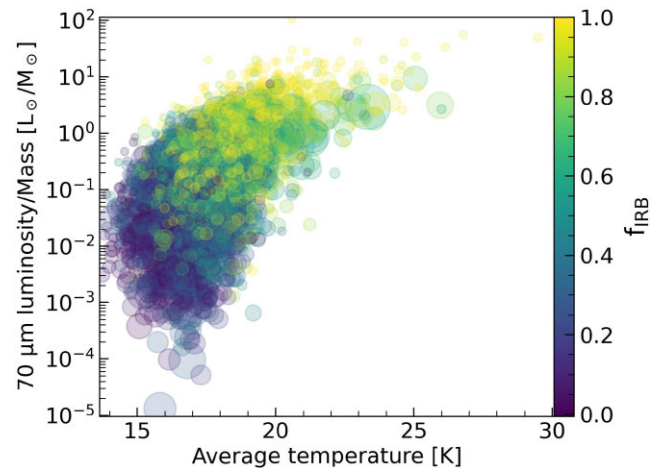

Figure 5. 70 μm luminosity to cloud mass against average dust temperature of all clouds with at least one 70 μm source. The colour of the markers indicate their f_{IRB} values and the size of each marker indicates their angular size on the sky.

the angular area of each molecular cloud to investigate additional factors that could influence the relationship. We note here that only 48 per cent of clouds had compact 70 μm sources. The figure shows that f_{IRB} correlates with both properties, strongly confirming f_{IRB} ability to trace how evolved the star formation is in molecular clouds.
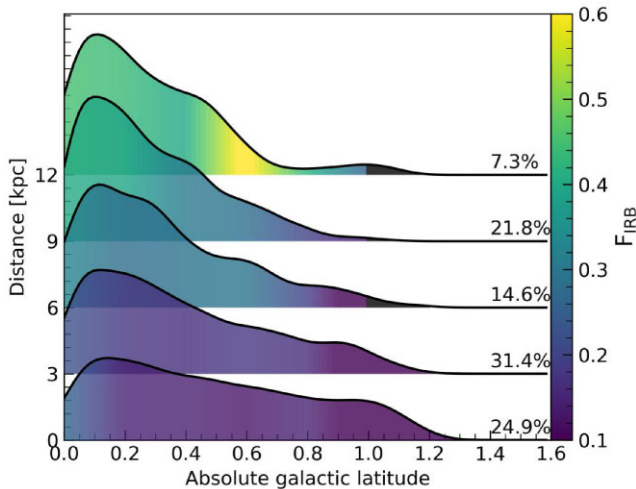
Figure 6. Kernel density estimations of molecular cloud distribution as a function of their Galactic latitude for five distance bins and are coloured by their median f_{IRB}. Note that the colourmap range is smaller than Fig. 5 to enhance contrast. Black indicates a parameter space that contained no clouds. Percentages indicate fraction of clouds contained at each distance.

We also see that the 70 μm luminosity over cloud mass values of clouds with larger areas have lower f_{IRB} than smaller clouds. This hints that there are secondary correlations that impact f_{IRB}.

4.2 How low background values affect f_{IRB}

The bright and dark regions at 8 μm are created by two different physical mechanisms. The bright regions are created by the additional photons produced by star formation, which causes them to always appear brighter than the background. But infrared dark features depend on both the background and foreground emission along the line of sight. Therefore, when the background emission is close to zero, the contrast between the Galactic background and the infrared dark molecular clouds is low, meaning they are more likely to be undetected or be detected with an overestimated f_{IRB}. Clouds at higher latitudes or at larger distances will be the most affected since 8 μm background will be lower. Using a high column density threshold to catalogue clouds and using a median filtered background to calculate f_{IRB} minimizes this bias but we cannot rule out that is has no impact in our catalogue.

To test whether f_{IRB} is impacted by distance or latitude, we plot these two quantities against each other on Fig. 6 as a ridge-line plot using a kernel density estimation (KDE). Since clouds are expected to have lower distances at higher Galactic latitudes (due to scale height of the disc), we split the clouds into 3 kpc bins so that each KDE shows the distribution of Galactic latitude between 0 and 3 kpc, 3 and 6 kpc, etc. We also colour each KDE by the median f_{IRB} binned in 0.2 deg latitude bins and linearly interpolate for a smoother visualization. Excluding the final distance bin, Fig. 6 reveals that f_{IRB} *decreases* as the latitude increases (i.e. as the background emission decreases), indicating that the decreasing background does not make the clouds appear more infrared bright. It implies that the star formation within clouds is slightly less evolved at higher latitudes (Planck Collaboration XXIII 2011; Planck Collaboration XXVIII 2016; Xu et al. 2024). The figure also shows that f_{IRB} does increases with distance.

To investigate if distance bias is responsible for increasing f_{IRB}, we plot the position of each cloud projected on top of the Milky

Way in heliocentric coordinates and label each cloud marker by its f_{IRB} on Fig. 7. While f_{IRB} increases with distance, the spatial information indicates that clouds with projected distances forming arc-like structures, which likely reflect spiral arm features, also have higher f_{IRB}. It also shows that in between the arm-like features (clouds in 'interarm' areas) f_{IRB} is lower. For example Sagittarius-Carina arm at $\ell \sim 300°$ reveals that f_{IRB} is high for both nearby and farther distances (on Fig. 7). To quantify this trend, we overplot two histogram insets on Fig. 7 in Galactocentric coordinates instead between $\ell = 20–40°$ and $\ell = 320–340°$ and colour the distance bins by the median f_{IRB}. These longitude ranges include both arm and interarm environments and are able to show that f_{IRB} increases for clouds found on expected arm locations while decreasing in-between them. Finally, we plot the change in f_{IRB} as a function of Galactic longitude as a histogram similar to before on Fig. 8. The figure shows when there is a long stretch of spiral arm or a long stretch of interarm on Fig. 7 over a narrow Galactic longitude range, f_{IRB} is higher or lower, respectively. Again, the increase in f_{IRB} is especially true for the Sagittarius-Carina arm at $\ell \sim 300°$.

Altogether, these figures reveal that there is an increase in f_{IRB} as a function of distance, but we are unable to determine the exact contribution that observational bias has on this trend because the occurrence of arm environments also increases with distance. However, we can say that there are physical causes that must play a role in increasing f_{IRB} with distance, considering we see environmental correlations, and considering that the weaker contrast present at higher latitudes does not cause f_{IRB} to increase. For further discussion on the impact distance bias might have on the following results, see Appendix B.

5 CLOUD PROPERTIES AS A FUNCTION OF THEIR f_{IRB}

5.1 Measuring cloud properties and their trends

For each cloud, we first calculate their distance-independent properties such as their projected angular area, their peak and mean column densities (N_{peak}, $\overline{N}$), their peak and mean dust temperatures (T_{peak}, $\overline{T}$) and their aspect ratio, AR using their moments. Using the assigned distance, we then calculated the total cloud mass and their effective radius, r_{eff}, given by

$$r_{eff} = \left(\frac{A_{cloud}}{\pi} \right)^{1/2}, \tag{1}$$

where A_{cloud} is the cloud area. Using the effective radius, we also estimate the mean spherical number density of each cloud. We then calculate their mass using the same molecular weight used in Peretto et al. (2016) of 2.8. After assigning cloud properties, we find a small number of clouds had no assigned number, or infinity for properties such as their mass, or their column density. These are caused by unassigned, or infinite values within the *Herschel* maps when saturation occurred in the observation itself. This removes an additional 405 clouds from our sample. Our final working sample is therefore 12 261.

To confirm that we are tracing physically realistic clouds, we compare the masses we derive to the CHIMPS catalogue (Rigby et al. 2019). CHIMPS is a molecular cloud catalogue that identified clouds using 15″ resolution ^{13}CO (3–2) data between $27.8° \leq \ell \leq 46.2°$ and $|b| \leq 0.5$ using the FellWalker (Berry 2015) algorithm (see Rigby et al. 2019 for more details). CHIMPS represents the ideal comparison set since ^{13}CO (3–2) traces higher column density
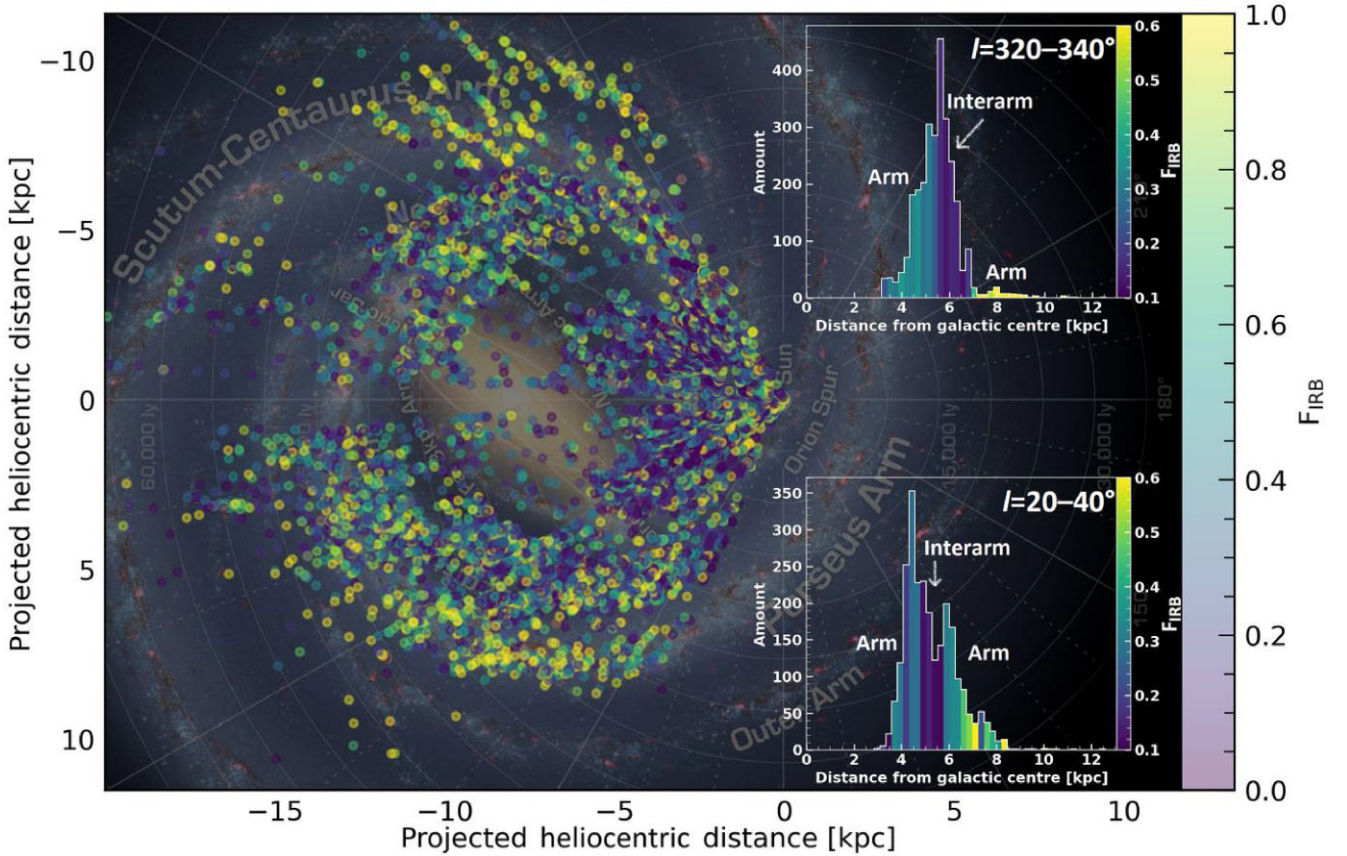
Figure 7. f_{IRB} of molecular clouds overplotted over the Milky Way. The colour of the markers represent the f_{IRB} of each cloud shown. Inset figures show the cloud number distributions and median f_{IRB} per bin in a narrow longitude range indicated on the inset to emphasize arm to interarm differences. We note here that the very circular distribution of a number of clouds as a function longitude at the tangent point is not real but caused by clouds being assigned the radial velocity at the tangent point if their radial velocity surpassed this value (Roman-Duval et al. 2009).
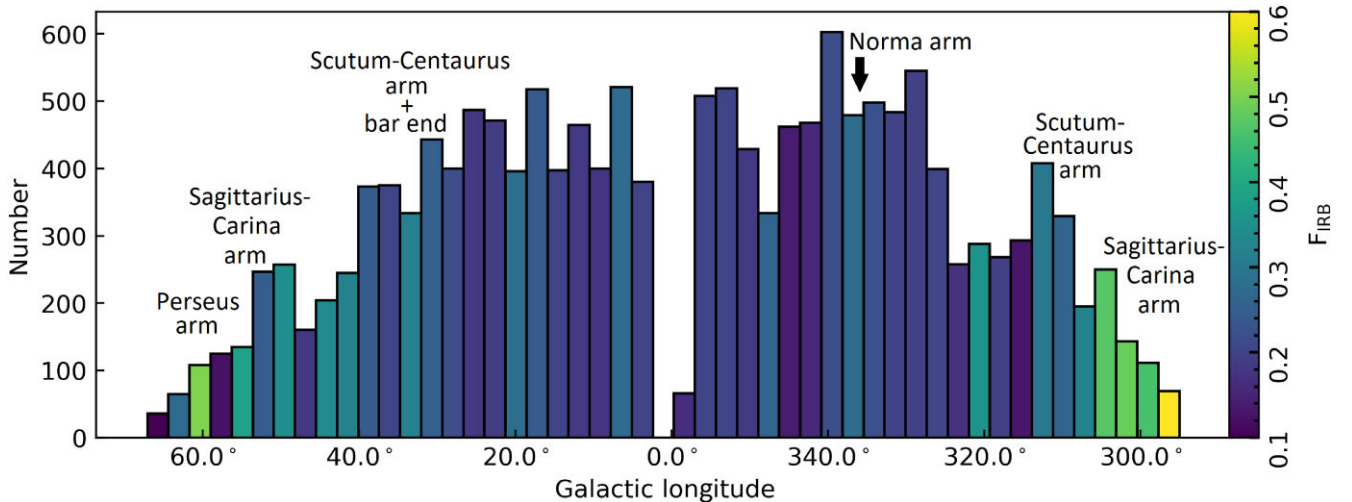

Figure 8. Histogram distributions of f_{IRB} of molecular clouds as a function of galactic longitude. Bins are coloured by their median f_{IRB}. Expected positions of arms from Fig. 7 with narrow longitudes along the line of sight from the Sun are indicated on the plot.

structures, which Rigby et al. (2019) results in them identifying clouds with sizes and densities intermediate between small- and large-scale molecular clouds. We cross-match the two catalogues only using the CHIMPS clouds that had a reliable flag. To cross-match, we use the central coordinates of both with a radii of 21″

each, matching the smoothing scale used to generate our catalogue in Section 3.1. We find 1115 out of 3664 CHIMPS clouds overlap with our catalogue and we plot their mass on Fig. 9 using the distances derived in Section 3.2. We find the two have good correspondence with the one-to-one line. Using Kendall's Tau, we find they have
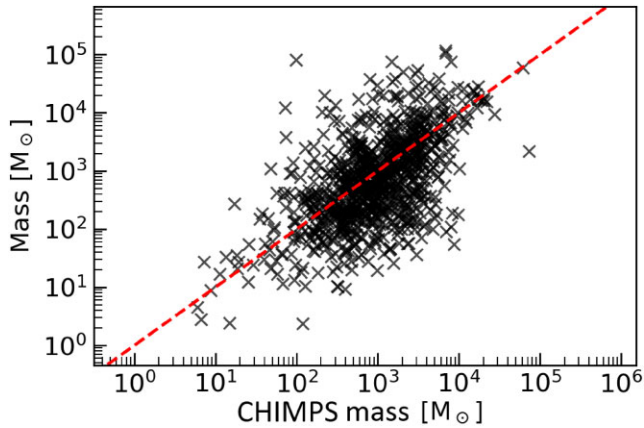
Figure 9. Mass of our catalogue against matched clouds from the CHIMPS catalogue (Rigby et al. 2019). Dashed red line shows the one-to-one line.
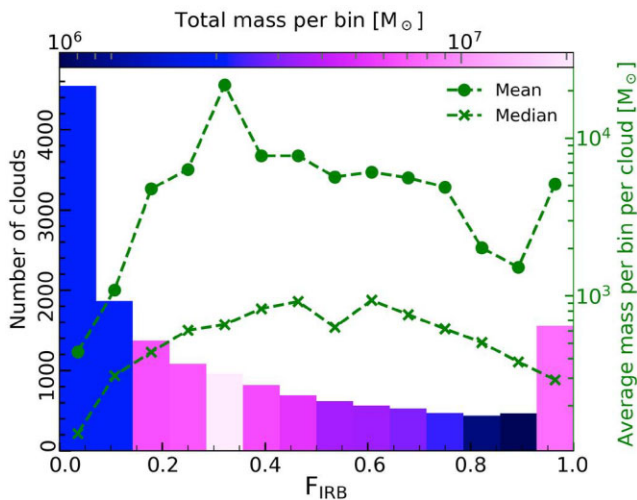

Figure 10. Distribution of f_{IRB} values with bins coloured by the total cloud mass within that bin. Overplotted in green lines are the average mass of clouds per bin. The circle markers show the mean values per bin. Cross markers show the median mass per bin.

a correlation of 0.40 with a *p*-value of 8.8×10^{-69}; therefore, we are confident our catalogue is representative of molecular clouds at higher column density thresholds.

Next, we explore the distribution of f_{IRB} and how it relates to the cloud properties. Even though clouds are dynamic and likely interchange mass via collisions and mergers during their lifetime (Jeffreson, Semenov & Krumholz 2024), for simplicity, in this section we assume that f_{IRB} linearly traces the lifetime of star-forming molecular clouds. We also assume our catalogue contains enough independent star-forming regions so that each phase is statistically well sampled. Under these assumptions, we expect an even number of bright and dark clouds. But when plotting the histogram distribution of f_{IRB} on Fig. 10, we find more clouds are infrared dark than bright. For example, 71 per cent of clouds possess $f_{IRB} < 0.5$ and the lowest bin (f_{IRB} between 0 and 0.07) represents 27 per cent of the catalogue. These results imply clouds spend more time starless. We also see that many clouds that have f_{IRB} values in the lowest f_{IRB} bin contain average column densities close to 1×10^{22} cm^{-2}. These clouds represent the highest column density peaks from a sample of more extended, lower density clouds that our

high column density cloud identification threshold excludes. Lower density clouds have longer free-fall times and so remain starless for longer, providing an even stronger argument for a longer starless period.

Similar results using f_{IRB} were also found in Rigby et al. (2021) who found the 75 per cent of clumps have $f_{IRB} < 0.663$. In addition, Battersby et al. (2017) also show that the infrared dark stage contains more gas and by using nearby maser measurements, they were able to assign lifetimes to these stages to confirm that the lifetime of infrared bright gas (i.e. gas containing star formation) is shorter than infrared dark gas. Observations that also characterize SFE per free-fall time (ε_{ff}) indicate ε_{ff} increases with as clouds age (Lee & Hennebelle 2016). With f_{IRB} correlating with SFE in Fig. 5, our results are consistent with a longer quiescent phase.

We next investigate how the mass is distributed within these bins, including the total mass per bin in Fig. 10, the mean mass per bin and the median mass per bin. Both the total and mean mass per bin peak when f_{IRB} is at intermediate values at around $f_{IRB} \sim 0.35$, not at 0, and the median mass per bin peaks at $f_{IRB} \sim 0.5$. The difference between the mean, median and total indicates that a small number of clouds have a much more rapid growth phase that skews the mean (and therefore increases the total mas per bin) to higher mass values. If clouds are isolated objects, we expect them to have more mass when their star formation is unevolved, more so considering that the majority of clouds in our sample are at starless stages (a quarter of the entire sample has $f_{IRB} < 0.07$). Then as stars evolve, stellar feedback is predicted to remove the gas. Instead, these results show that on average, all clouds gain molecular gas as star formation progresses rather than losing mass, at least until 50 per cent of their area has star formation. The decrease in number distribution of clouds on Fig. 10 also implies that the rate of mass gain must accelerate in time. In summary, these results show molecular clouds are not isolated but instead grow in mass over time while forming stars.

5.2 Exploring data trends using PCA analysis

Results presented previously in this section, and Section 4 indicate there are secondary correlations impacting the cloud properties. For example, Fig. 5 has a secondary correlation relating to the cloud size. To explore the correlations between the cloud properties, and to optimize how trends are displayed, we perform principal component analysis (PCA) on the cloud properties. PCA is a multivariate method that linearly combines a set of variables along successive, orthogonal axes to maximize the variance of the data set. PCA implicitly assumes data linearity and that the components are orthogonal, both of which are needed for simple, solvable PCA solutions. It also assumes that data variance represents information, so variables with larger variances are more important and necessary to explain the data. By projecting the data along these new axes – their principal components – we are maximizing the information we can access (i.e. where a small increase or decrease in the variables result in the largest change in the cloud properties). This allows us to reduce the dimensionality of the data by removing principal components we know contain the least variance, which simplifies data trends while retaining the most amount of information possible. It also projects the data along the axes that maximize the variance, which maximizes the visibility of any trends present.

The principal components are calculated by scaling the data, finding the eigenvectors of the data covariance matrix, and ordering them according to their eigenvalues, from largest to smallest. The data are then converted to their principal component scores by projecting the data to this eigenbasis. The eigenvectors, $\boldsymbol{v}_i$, therefore point in

Table 1. Table showing the eigenvectors of all five principle components (and their physical interpretation) for each variable. Values close to 0 indicate little contribution from the variable to the principle component, while values close 1 or −1 indicate strong contribution from the variable.

Variable	PC1 (Evolution)	PC2 (Size)	PC3 (Symmetry)	PC4 (Diffuseness)	PC5
Peak column density	0.29	0.55	−0.03	−0.78	−0.10
Cloud mass	0.08	0.57	0.71	0.40	0.04
Average temperature	0.68	−0.10	−0.09	0.10	0.71
IR brightness fraction	0.66	−0.15	−0.04	0.23	−0.69
Aspect ratio	−0.06	0.59	−0.70	0.41	−0.00
Explained variance	30 per cent	21 per cent	20 per cent	18 per cent	11 per cent

the direction of the principal components while the absolute value of eigenvalues $|\lambda_i|$, which we normalize so that their sum equals one – explains the variance that component represents.

Before we perform PCA, we first eliminate variables that are directly derived from a more fundamental variable to ensure data orthogonality, such as the number density, which is derived from the mass and the physical cloud area. The mass also depends on the distance and the physical area so there will be no new information gained by including the last two variables. Additionally, both the average and peak temperature, and the average and peak column density are highly correlated parameters, information we know and expect. Including them paired together will skew the PCA towards them. After testing the peak and average values separately using PCA, we find that the average temperature, and the peak column density produced stronger components. Altogether, we performed PCA using f_{IRB}, the peak column density, the average temperature, the cloud mass and the aspect ratio of the clouds and tabulate the eigenvectors (i.e. the principle directions) and their absolute normalized eigenvalues (i.e. their explained variance) in Table 1.

Our first check is to find and remove principal components that only explain a small fraction of the data variance to simplify the interpretation and visualization of the data. We find that there is no single component that explains the majority (∼90 per cent) of the variance, which would greatly simplify our interpretation. Instead, we find that the almost all the data variance can be explained with the first four principal components, cumulatively representing 89 per cent of the data variance and show this in Table 1. As a result, we remove component five and project the data without it. With the four remaining components, we interpret the correlations shown in Table 1. Table 1 shows the following:

(i) The first principle component (PC1) is dominated by f_{IRB} and the average temperature, with a small contribution from the peak column density. Since f_{IRB} and the temperature trace evolution, we call PC1 the 'evolution' axis.

(ii) PC2 traces the mass, peak column density and the aspect ratio of the clouds, all of which are size related parameters. Objects with more mass tend to reach higher column densities and so we call this axis the 'size' axis.

(iii) PC3 traces a strong anticorrelation between mass and aspect ratio. This component likely shows that spherical clouds contain more mass than filamentary clouds when both have the same column density (i.e. spherical clouds have a larger area). As a result, we call this axis the 'symmetry' axis.

(iv) PC4 shows that an increase in the mass and the aspect ratio results in a decrease in peak column density. The physical interpretation we infer is rounder objects require less mass to reach higher peak column densities. Therefore, we call this axis the

'diffuseness' axis so that negative values indicate a cloud that is more centrally concentrated.

Potentially, PC3 and PC4 both indicate that spherical clouds are more efficient at concentrating mass, which was also found in Rigby et al. (2018).

To explore how the cloud properties relate to the four principal axes, we plot the cloud scores projected along all four principal axes on Fig. 11. We plot the diffuseness against the symmetry axis and colour the markers by their evolution and change the marker size to show the size axis. The graph shows that clouds have a distinct location as a function of their morphology and evolutionary state. We find the youngest, and least evolved clouds on a narrow horizontal band. Their position in respect to the symmetry and diffuseness axis indicate that the youngest clouds have a range of aspect ratios, though clouds with high aspect ratios (i.e. more filamentary) have lower peak column densities but contain more mass.

However, the most interesting trend on Fig. 11 is how the symmetry and diffuseness change as the clouds evolve. First, we see that clouds appear to become more evolved with different properties. The clouds that evolve down and left on the figure get larger, become more centrally concentrated (increase their peak column density), but become less symmetrical. The clouds that evolve up and right on the figure only increase their mass and peak column density slightly as they evolve and the rightward direction means they also become slightly more symmetric.

To better understand this evolutionary trend and how it relates to the physical cloud properties, we calculate the median mass, peak column density and f_{IRB} in parallel strips (i.e. bins) away from the evolutionary minimum, which is indicated using the thin solid black line on Fig. 11. Each parallel strip contains an equal number of clouds. We plot these averages on Fig. 12, where the y-axes on the top and bottom panels show the median mass and peak column density, respectively, while the x-axis shows distance away from the evolutionary minimum. A value of zero on the x-axis of Fig. 12, therefore, represents the centre of the evolutionary minimum, negative values show clouds that evolve downwards on Fig. 11, and positive values show clouds upwards. The marker colours show the median f_{IRB} values.

Fig. 12 shows that the cloud properties bifurcate. While both directions show clouds grow as star formation occurs, the clouds that evolve vertically upwards (positive values on the x-axis of Fig. 12) gain up to ∼4 times their starting mass, while their peak column densities only reach a factor of 1.3 times their starting value on average as f_{IRB} increase. After $f_{IRB} > 0.5$, the total mass decreases but their peak column density remains constant until the cloud becomes $f_{IRB} \simeq 0.9$ where their peak column density finally begins to decrease. Potentially, this shows that when dense gas forms, it is more resilient to being removed, while the more diffuse mass can be removed after the clouds become star forming (Watkins et al. 2019). The majority of clouds (which we refer to as 'small clouds') follow these average evolutionary properties, representing ∼80 per cent of the catalogue. Indeed, the mass resembles the median averaged cloud mass per f_{IRB} bin on Fig. 10.

This is the simple, standard scenario that might be expected for the star-forming clouds: clouds collapse due to gravity to form stars, and then are destroyed by the feedback the stars produce. Our results add that the clouds continuously accretes material while forming stars, and this halts only after 50 per cent of the cloud area is star forming. However, a more isolated view of star formation is especially unsuited in 20 per cent of cases. These clouds gain significantly more mass (a factor of ∼150 times more) and reach
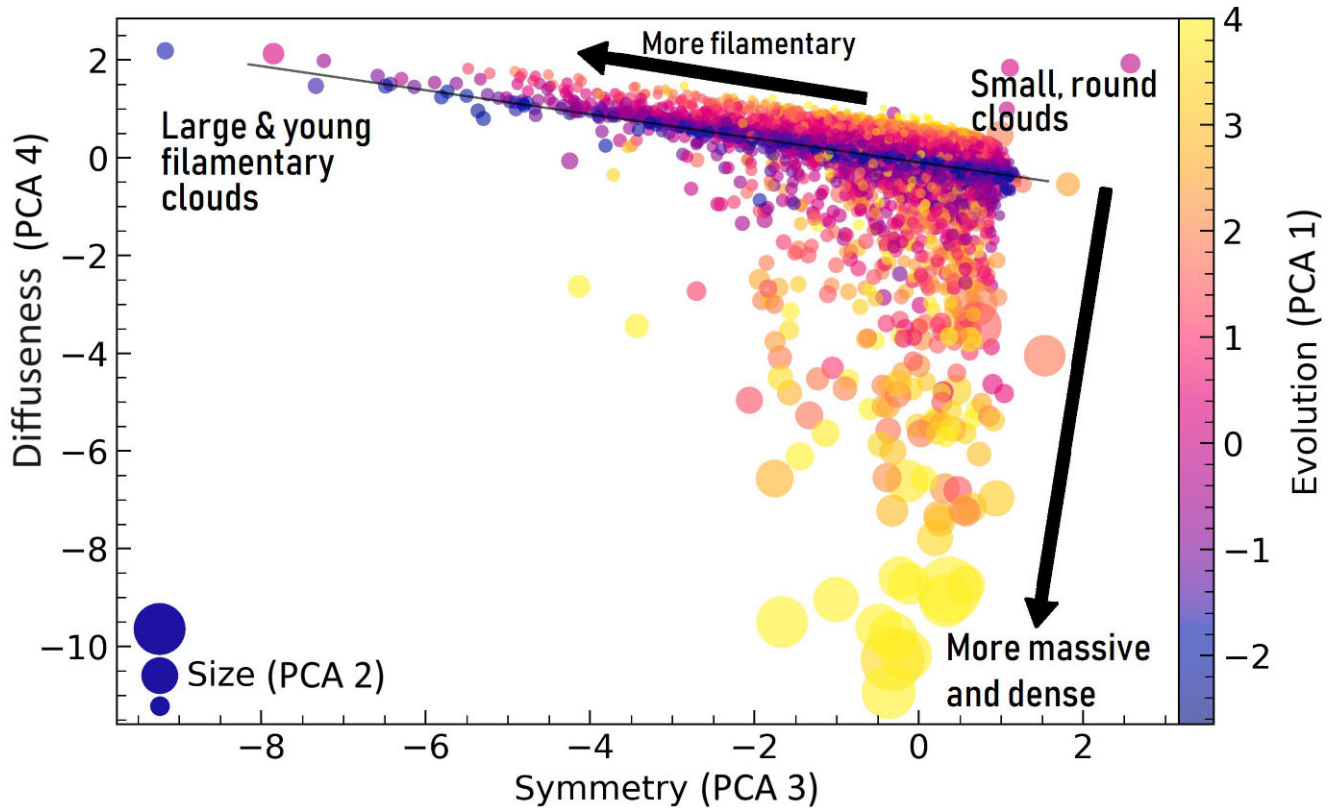
Figure 11. Score plot of the cloud catalogue using their principal components. The diffuseness axis (PC4) is represented using the *y*-axis, the symmetry axis (PC3) is represented using the *x*-axis, the marker colours represent the evolution axis (PC1), and the size of the markers shows the size of the clouds (PC2). This black line illustrates the evolutionary minimum. Annotations indicate the cloud properties present at those plot locations.

much higher peak column densities (becoming 40 times more dense) as f_{IRB} increases. In fact, Fig. 12 reveals that in the beginning, the average f_{IRB} value *decreases* slightly for the high-mass clouds. This suggests that initially, mass rapidly accretes on to these clouds at a rate that outpaces the initial star formation occurring within the clouds. While weaker, the same trend can be seen in Fig. 5. The figure shows that clouds with a larger angular size have lower f_{IRB} than the smaller clouds. This shows how PCA is able to disentangle subtle trends by maximizing the variance.

Because these clouds are significantly larger (5 times more massive on average), they represent 55 per cent of the mass contained in this survey. Assuming that all clouds have the same SFE, it indicates that half of all star formation in our sample occurs within this small population of molecular clouds. As a result, we refer to these clouds as 'large clouds'. Miville-Deschênes, Murray & Lee (2017) and Urquhart et al. (2018) also show that most of the star formation within the Milky Way is found in a small number of massive star-forming complexes.

While we see the cloud growth on Fig. 10 and discuss it in Section 5, to confirm that there is two different amounts that clouds grow by (and is not an artefact of the PCA projection), we plot the histogram distributions for peak column density and mass, and colour the bins by their median f_{IRB} per bin for the two cloud types in Figs 13 and 14. The two plots show that there are distinct differences in both the distribution of values and the median f_{IRB} for the two cloud types. For example, Fig. 13 shows that the bigger clouds have much lower f_{IRB} when peak column densities are small and have a much larger tail for high values. We end this section by noting that we investigate if our previous analysis impacts the PCA results in Appendix B.

In particular, we check if the bifurcation could be caused by the cloud merging algorithm used in Section 3.1, if any of our results are impacted by the distance assigned, and if the potential distance bias (discussed in Section 4.2) impacts the PCA. Our investigations show that our analysis does not impact the PCA results.

5.3 Environmental trends

Here, we explore potential trends in cloud properties versus environmental features and discuss the implications of our results. We note that since the location of spiral arms, or even the number of arms is are still a matter of debate, and kinematic distances can be problematic (Reid 2022) the analysis we can perform is limited. Therefore, we do not compare against any particular model other than the Milky Way visualization as an aid to the discussion and use the large-scale structure of our cloud catalogue projected on a face-down view to inform whether features are likely associated with arm or interarm environments.

In Fig. 7, we find that f_{IRB} increases in clouds grouped together into arc-like features, which when overplotted on a face-down visualization of the Milky Way, show alignment with spiral arm features. We also show that between these arcs, f_{IRB} of clouds decreases in visual agreement to more interarm environments. This is more easily seen on Fig. 15 where we plot the spatial distribution of our clouds that have $f_{IRB} < 0.1$ or $f_{IRB} > 0.90$. We can see how the most evolved clouds cluster together into thin arcs and, more often than not, between these arcs are the less evolved clouds. If we assume that all clouds goes through the entire range of f_{IRB} values during their lifetimes, Fig. 15 shows that the relative duration of
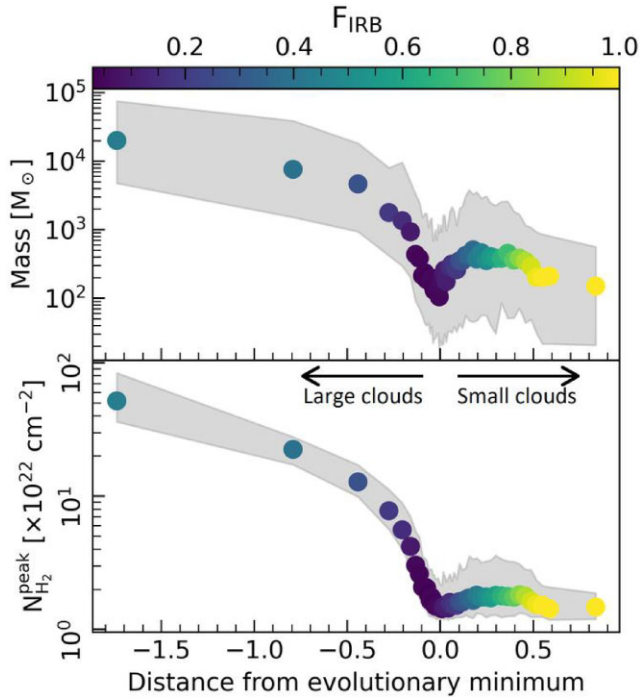
Figure 12. Median cloud properties as a function of evolution. Median calculated using equal number of clouds binned as a function of distance perpendicular from the evolutionary minimum represented as the black line on Fig. 11. Therefore, negative values show the change in cloud properties as a function of evolution for clouds that fall below the evolutionary minimum and positive values show the same but for clouds above. *Top panel* are median mass values and *bottom panel* are median peak column density values. The marker colours show the median f_{IRB} and the grey-shaded region show the 16–84 per cent sigma spread in the mass and peak column density.
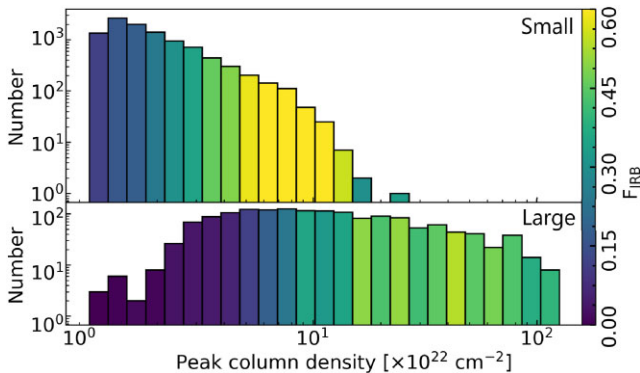
Figure 13. Histogram distribution of peak column density values for *large clouds* and *small clouds*. Bins coloured by the median f_{IRB} per bin for the two cloud types revealed in Fig. 11. *Top panel* are small clouds (clouds that evolve above the line on Fig. 11) and *bottom panel* are large clouds (clouds that evolved below the line instead). Size of the *y*-axis on both panels use the same scale to better compare the distributions.

the different phases changes as a function of Galactic location. This likely represents a difference in cloud mass growth, implying the larger scale structure influences how molecular clouds evolve.

In Appendix C, we further investigate the distribution of the two cloud types between the arms and interarm regions by plotting their top–down positions on Figs C1 and C2. These figures show that the large cloud distribution form tight extended arc-like structures that
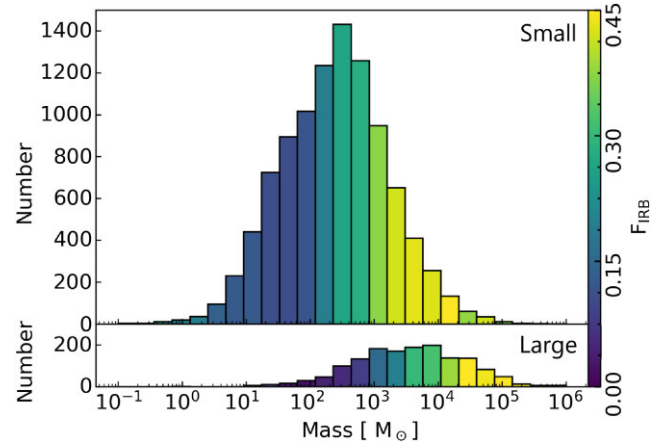
Figure 14. Same as Fig. 13 but for mass.

congregate to the expected positions of the spiral arms illustrated on the visualization of the Milky Way. Furthermore, the face-down distribution shows that the arcs are separated by gaps. The lower mass clouds do not have as strongly delineated arc features, appearing everywhere, though they still cluster into arc-like features and we visually see small clouds before an arm-like feature have lower f_{IRB} values, and larger f_{IRB} on and after it. The large clouds therefore seem to preferentially formed in spiral arms. This could be due to spiral arms enhancing the conditions necessary for their formation. For example, an increase in surface density of molecular clouds was also detected in Miville-Deschênes et al. (2017) using CO. However, we cannot yet rule out the large clouds being a random sampling of the small cloud distribution given their more limited numbers.

6 DISCUSSION

6.1 Molecular cloud growth during star formation.

From Fig. 14 it is clear that both the small and large clouds have greater masses when f_{IRB} is higher. This suggests that both populations of clouds are growing in mass *at the same time* as they are undergoing star formation. Let us now consider how the cloud mass and star formation evolve for both types of clouds.

We find that small clouds grow by four times their original mass as their star formation evolves. While the exact mechanism for this growth is unclear, it can be explained easily by cloud collisions or by clouds accreting the surrounding lower density H_2. The time-scale for cloud–cloud collisions is simulated to be 8–10 Myr in spiral galaxies (Dobbs et al. 2015). If we estimate that small clouds recycle their mass at least every 40 Myr from the feedback injection time-scale from clustered supernovae (Orr et al. 2022) they would be expected to collide ~4 times over their lifetime, matching the expected grow rate we see. We can also explain the growth by assuming the small clouds accrete the surrounding gas. If it accretes the surrounding 1×10^{21} cm^{-2} column density gas within a 3 pc volume, we can achieve mass growth rates matching our results. However, what is more difficult to explain is why they only gain four times their mass. Potentially, if only part of the structure is gravitational bound and able to form stars, they will not effectively convert their gas into stars. Moreover, their diffuse nature may make them more easily disrupted by external forces such as supernovae (Feng et al. 2024) or tidal forces (Ramírez-Galeano et al. 2022). Thus, the lowest mass part of the sample may never evolve into massive clouds.
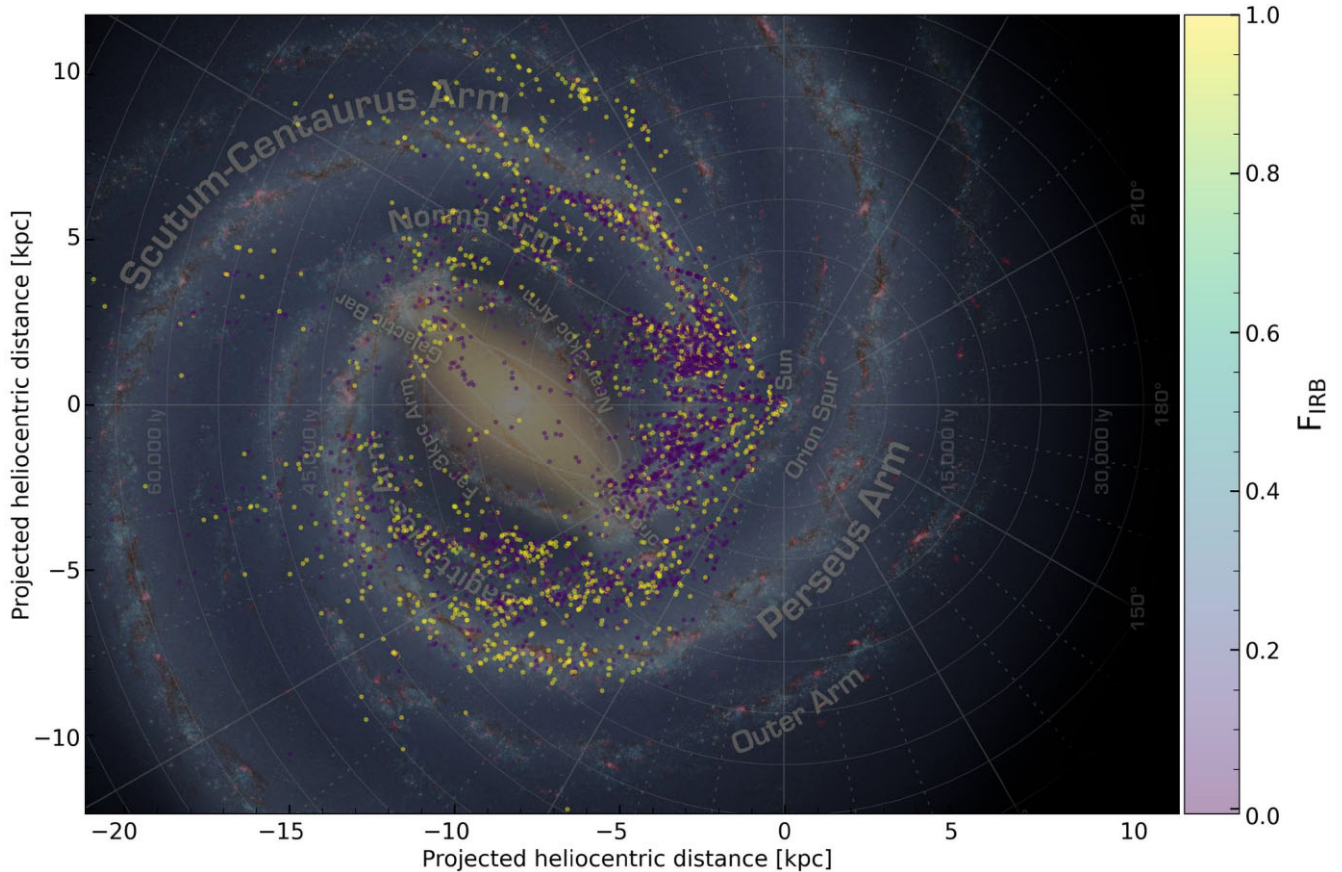
Figure 15. f_{IRB} of molecular clouds overplotted over the Milky Way only for clouds with high (>0.90) and low (<0.1) f_{IRB} values. Blue markers show low f_{IRB} clouds while yellow show the high f_{IRB} clouds.

Similar growth arguments are harder to apply to large clouds. One scenario is that the large clouds form from a single larger scale instability. Therefore, we might be witnessing clouds condensing at a higher mass via gravitational instabilities directly from the H I in the high potential environment of the spiral arms (Meidt 2022). It is from this state they could continue to grow into the large clouds we find in this survey. Large clouds could also represent where H_2 formation occurs in a non-equilibrium state (Burkhart et al. 2024). These authors show molecular clouds can gain over a factor 100 times more mass, while star formation is ongoing. In particular, we note that the mass growth curve shown in their fig. 1 is remarkably similar to the mass growth we see in Fig. 12. Recent simulations from Dobbs, Burkert & Pringle (2011) and Jeffreson et al. (2024) also show that molecular clouds were found to persist for long periods (up to 90 Myr) despite rapid star formation within them due to fresh accretion of gas and due to mergers with smaller clouds.

Our results favour the latter scenario. We show there is a clear difference in the column density evolution of the two cloud samples shown in Fig. 13. The small clouds decrease in number as the peak column density increases. This is consistent with single objects undergoing free-fall collapse, where the evolutionary time-scale is shorter at higher densities. However, the large clouds have a much flatter distribution of peak column densities, with less clouds with low peak column densities, which also have lower f_{IRB} values. This suggests that the clouds are gaining fresh mass as regions within them are collapsing. This would replenish the cloud with new infrared dark

gas allowing f_{IRB} to remain low while the cloud itself continues to grow to higher masses and column densities. Finally, the absence of high f_{IRB} can be explained by the rapid destruction of the clouds once star formation finally outpaces the mass growth. The high-mass cloud likely consumes and destroys the remain gas, halting mass accretion. As a result, it no longer meets the properties needed to be identified as a large cloud (which is likely responsible for the increase in massive highly evolved star formation in Fig. 10). This also matches the evolutionary path outline in Burkhart et al. (2024). They show that cloud growth halts only when enough stars form that they destroy the H_2 faster than the mass gain. We therefore expect large clouds would preferentially form in environments where there is a large gas reservoir, crowding of orbits to facilitate merging of clouds, and a deep potential well to encourage large-scale collapse. Such an environment may be found in spiral arms.

Dynamic star forming processes have been predicted before (Lee, Miville-Deschênes & Murray 2016; Kobayashi et al. 2017; Vázquez-Semadeni et al. 2019). For example, Lee et al. (2016) found star formation rates increase over time, which may be explained by clouds growing and collapsing while forming stars. These results have strong implications on how we assess the star-forming efficiency within a region, and the final number of stars a cloud produces. The mass we use to judge a cloud properties, such as the number of stars it can produce, can be misleading if clouds grow over time alongside their star formation. Furthermore, if the cloud has recently accreted a significant amount of mass faster than it forms stars, we would predict that it has a low SFE per free-fall time.

6.2 How large-scale structure impacts cloud properties

In the previous section (Section 5.3), we raise the possibility that there may be a change in the evolution of star formation, as traced by f_{IRB} in the vicinity of spiral arms. For example, the histogram insets on Fig. 7 hints that the clouds that gather into arc-like structures have more evolved star formation than the rest of the galaxy. The top–down view of the least and most evolved clouds on Fig. 15 also hints at this relationship assuming that the long arc-like structures that the projected cloud positions create are spiral arms. Since the exact positions of spiral arms are highly debated, the following discussion does not use a spiral arm model. More importantly, after testing different spiral arm models, small offsets between our catalogue and the model made analysis inconclusive. Due to these observational limitations, our results and the following discussions are tentative but if present, they reveal that the organization of gas on large-scale impacts not only how clouds evolve, but where they evolve.

We weakly find on Fig. C1 that denser environments where we detect more clouds in a smaller area, such as large-scale spiral-arm-like structures, are a pre-requisite for creating the large cloud population. Physically, this could mean that spiral arm-like locations allow some clouds (i.e. the large clouds) to grow more massive due to deeper potential wells or access to more gas. Or, due to the source blending at spiral arm locations, we are detecting more column along the line of sight over a small spatial area, resulting in higher masses and higher peak column densities. While we cannot eliminate source blending, we do minimize it by excluding regions that contained too many different distance and velocity values (see Section 3.2). Furthermore, the background filtering performed on the column density maps removes material that would contribute to the source blending. Finally, since we also detect a lot the small clouds in spiral arms locations, we expect both cloud types should be impacted by source blending, meaning that differences between these two populations of clouds should be independent of the source blending. Irregardless of the dominant reason, the larger-scale spiral arm structure is likely bringing gas together in such a way that we detect a significant amount of star formation from a small area that will eventually result in larger stellar associations in that small area.

Changes in clouds properties between interarm and spiral arm molecular clouds have been shown before in the Milky Way (using CO) at similar spatial resolutions (Moore et al. 2012; Sawada et al. 2012; Rigby et al. 2019) and in nearby galaxies with well-defined spiral structure at larger spatial scales (Colombo et al. 2014; Faustino Vieira et al. 2024). In particular, Sawada et al. (2012) and Colombo et al. (2014) found two cloud populations that correlate with environment in a similar way to our work. They found that clouds in the interarm tend to be lower mass and have lower contrasts between strong and weak emission, but also indicate these clouds can exist within the spiral arms, which matches our results. Furthermore, they also found that the second population of clouds with high contrasts and higher masses primarily located in spiral arms.

To truly determine the mechanism that dominates the cloud growth of large clouds, tracing the surrounding H I in relation to the molecular gas, surveying out to the outer galaxy to compare cloud growth in a lower density environment (Beuther et al. 2016; Soler et al. 2020), and using Milky Way simulations resolving down to $100\,M_\odot$ to estimate cloud collision time-scales and H I environments (e.g. Dobbs et al. 2015; Smith et al. 2023) in the spiral arms are needed.

7 CONCLUSIONS

In this paper, we traced how evolved the star formation is within $\sim$12 000 molecular clouds to test how cloud properties change as star formation progresses. We identified these clouds by applying a column density cut of 1×10^{22} cm^{-2} *Herschel*–Hi-GAL column density maps between $|\ell| < 70°$ and $|b| < 1°$. To measure the evolutionary state of clouds, we calculated their infrared bright fraction, f_{IRB} using *Spitzer* GLIMPSE 8 µm observations. This fraction corresponds to the fraction of a cloud that is 8 µm against the background emission and traces the relative evolution of clouds due to the fact that 8 µm emission can represent both starless, and star-forming gas when compared against a bright background 8 µm source.

f_{IRB} revealed that molecular clouds form stars simultaneously with their formation from the galactic environment. They gain mass and become denser despite their ongoing star formation. As a result, the final amount of stars that a region can form is not set purely by the initial amount of gas present in starless molecular clouds. To better view subtle secondary trends observed in cloud properties, we performed PCA. PCA revealed molecular clouds properties bifurcated down two evolutionary paths that reflected how much mass they gain as star formation progresses. Most molecular clouds (80 per cent) gain on average four times their original mass (termed small clouds) but the remaining 20 per cent per cent instead gain 150 times more mass (termed large clouds). As a result, both cloud types account for $\sim$50 per cent of the star formation occurring within the survey area.

Both cloud types eventually stop growing and begin losing mass, but only after half their area becomes star forming. We see the mass of small clouds decrease gradually, while their peak column density remains high. The stellar feedback from the recently formed stars likely removes their more diffuse gas when their dense centre remains star forming. Large clouds rarely surpass an f_{IRB} of 0.5. We predict large clouds break up into smaller clouds due to feedback (potentially in combination with additional disruptive forces such as shear), resulting in massive evolved fragments being identified in the small cloud category.

The rate of mass gain seen in small clouds can be explained via cloud–cloud collisions, or simply accreting the surrounding lower density gas. We expect the small-mass gain is caused by feedback limiting diffuse gas accretion quickly at early stages. Large clouds can achieve high-mass gain due to continuous accretion from flows external to the cloud that provides a fresh supply of H_2 that outpaces its removal from feedback processes. Clouds with access to higher density gas-rich environments, or higher gravitational potentials, such as spiral arms, likely provide the conditions needed for this rapid growth. We see tentative evidence for such environmental differences as we find f_{IRB} is higher and there are more large clouds in arm-like environments. However, until galactic structure and cloud distances are better constrained, we cannot yet confirm this.

Altogether, our results imply star formation is a quick but inefficient process at cloud scales due to stellar feedback limiting cloud growth. Their ability to grow in mass whilst forming stars also implies that we will underpredict the star forming ability of molecular clouds at early stages when treating them as static, isolated objects. This has far reaching implications on using a metric such as the SFE per free-fall time for cloud studies.

ACKNOWLEDGEMENTS

DATA AVAILABILITY

The data products underlying this article will be shared on reasonable request to the corresponding author.

REFERENCES

Abe D., Inoue T., Inutsuka S.-i., Matsumoto T., 2021, ApJ, 916, 83
Anderson M. et al., 2021, MNRAS, 508, 2964
André P., Di Francesco J., Ward-Thompson D., Inutsuka S.-I., Pudritz R. E., Pineda J. E., 2014, Protostars and Planets VI, 27
Battersby C., Bally J., Svoboda B., 2017, ApJ, 835, 263
Berry D. S., 2015, Astron. Comput., 10, 22
Beuther H. et al., 2016, A&A, 595, A32
Burkhart B. et al., 2024, ApJ, 975, 269
Chen C.-Y., Mundy L. G., Ostriker E. C., Storm S., Dhabal A., 2020, MNRAS, 494, 3675
Chevance M. et al., 2020a, Space Sci. Rev., 216, 50
Chevance M. et al., 2020b, MNRAS, 493, 2872
Churchwell E. et al., 2009, PASP, 121, 213
Clark P. C., Glover S. C. O., 2014, MNRAS, 444, 2396
Colombo D. et al., 2014, ApJ, 784, 3
Colombo D., Rosolowsky E., Ginsburg A., Duarte-Cabral A., Hughes A., 2015, MNRAS, 454, 2067
Dobbs C. L., Burkert A., Pringle J. E., 2011, MNRAS, 417, 1318
Dobbs C. L., Pringle J. E., Duarte-Cabral A., 2015, MNRAS, 446, 3608
Dunham M. M., Crapsi A., Evans N. J. II, Bourke T. L., Huard T. L., Myers P. C., Kauffmann J., 2008, ApJS, 179, 249
Elmegreen B. G., 2011, EAS Publ. Ser., 51, 19
Evans N. J. II et al., 2009, ApJS, 181, 321
Faustino Vieira H., Duarte-Cabral A., Davis T. A., Peretto N., Smith M. W. L., Querejeta M., Colombo D., Anderson M., 2024, MNRAS, 527, 3639
Fazio G. G. et al., 2004, ApJS, 154, 10
Feng J., Smith R. J., Hacar A., Clark S. E., Seifried D., 2024, MNRAS, 528, 6370
Grisdale K., Agertz O., Romeo A. B., Renaud F., Read J. I., 2017, MNRAS, 466, 1093
Hopkins P. F., Kereš D., Oñorbe J., Faucher-Giguère C.-A., Quataert E., Murray N., Bullock J. S., 2014, MNRAS, 445, 581
Jeffreson S. M. R., Semenov V. A., Krumholz M. R., 2024, MNRAS, 527, 7093
Johnstone D., Francesco J. D., Kirk H., 2004, ApJ, 611, L45
Kobayashi M. I. N., Inutsuka S.-i., Kobayashi H., Hasegawa K., 2017, ApJ, 836, 175
Krumholz M. R., Klein R. I., McKee C. F., 2007, ApJ, 656, 959
Lee Y.-N., Hennebelle P., 2016, A&A, 591, A31
Lee E. J., Miville-Deschênes M.-A., Murray N. W., 2016, ApJ, 833, 229
Marble A. R. et al., 2010, ApJ, 715, 506
Mazumdar P., Wyrowski F., Urquhart J. S., Colombo D., Menten K. M., Neupane S., Thompson M. A., 2021, A&A, 656, A101
Mège P. et al., 2021, A&A, 646, A74
Meidt S. E., 2022, ApJ, 937, 88
Miville-Deschênes M.-A., Murray N., Lee E. J., 2017, ApJ, 834, 57
Molinari S. et al., 2010a, PASP, 122, 314
Molinari S. et al., 2010b, A&A, 518, L100
Molinari S., Schisano E., Faustini F., Pestalozzi M., di Giorgio A. M., Liu S., 2011, A&A, 530, A133
Molinari S. et al., 2016, A&A, 591, A149
Moore T. J. T., Urquhart J. S., Morgan L. K., Thompson M. A., 2012, MNRAS, 426, 701
Myers P. C., 2009, ApJ, 700, 1609
Orr M. E., Fielding D. B., Hayward C. C., Burkhart B., 2022, ApJ, 932, 88
Peretto N., Fuller G. A., 2009, A&A, 505, 405
Peretto N., Lenfestey C., Fuller G. A., Traficante A., Molinari S., Thompson M. A., Ward-Thompson D., 2016, A&A, 590, A72
Pettitt A. R., Dobbs C. L., Baba J., Colombo D., Duarte-Cabral A., Egusa F., Habe A., 2020, MNRAS, 498, 1159
Planck Collaboration XXIII, 2011, A&A, 536, A23
Planck Collaboration XXVIII, 2016, A&A, 594, A28
Priestley F. D., Clark P. C., Glover S. C. O., Ragan S. E., Fehér O., Prole L. R., Klessen R. S., 2023, MNRAS, 526, 4952
Ragan S. et al., 2012, A&A, 547, A49
Ragan S. E., Henning T., Tackenberg J., Beuther H., Johnston K. G., Kainulainen J., Linz H., 2014, A&A, 568, A73
Ramírez-Galeano L., Ballesteros-Paredes J., Smith R. J., Camacho V., Zamora-Avilés M., 2022, MNRAS, 515, 2822
Rani R., Moore T. J. T., Eden D. J., Rigby A. J., Duarte-Cabral A., Lee Y.-N., 2023, MNRAS, 523, 1832
Reid M. J., 2022, AJ, 164, 133
Rigby A. J. et al., 2018, A&A, 615, A18
Rigby A. J. et al., 2019, A&A, 632, A58
Rigby A. J. et al., 2021, MNRAS, 502, 4576
Rigby A. J. et al., 2024, MNRAS, 528, 1172
Roman-Duval J., Jackson J. M., Heyer M., Johnson A., Rathborne J., Shah R., Simon R., 2009, ApJ, 699, 1153
Rosolowsky E., Leroy A., 2006, PASP, 118, 590
Rosolowsky E. W., Pineda J. E., Kauffmann J., Goodman A. A., 2008, ApJ, 679, 1338
Sawada T., Hasegawa T., Sugimoto M., Koda J., Handa T., 2012, ApJ, 752, 118
Schneider S., Elmegreen B. G., 1979, ApJS, 41, 87
Smith R. J. et al., 2020, MNRAS, 492, 1594
Smith R. J. et al., 2023, MNRAS, 524, 873
Soler J. D. et al., 2020, A&A, 642, A163
Urquhart J. S. et al., 2018, MNRAS, 473, 1059
Vázquez-Semadeni E., Palau A., Ballesteros-Paredes J., Gómez G. C., Zamora-Avilés M., 2019, MNRAS, 489, 714
Watkins E. J., Peretto N., Marsh K., Fuller G. A., 2019, A&A, 628, A21
Watkins E. J. et al., 2023, ApJ, 944, L24
Werner M. W. et al., 2004, ApJS, 154, 1
Williams J. P., de Geus E. J., Blitz L., 1994, ApJ, 428, 693
Xu F. et al., 2024, ApJ, 963, L9
Zucker C., Battersby C., Goodman A., 2015, ApJ, 815, 23

APPENDIX A: ADDITIONAL FIGURES ILLUSTRATING MERGED CATALOGUE

In this appendix, we show two further examples of the cloud catalogue after applying the merging algorithm at two crowded locations in addition to the example shown on Fig. 2. The first example (see Fig. A1) shows the catalogue at the bar end at $\ell = 30°$ and the second shows the catalogue towards the galactic centre $\ell = 2°$ (see Fig. A2). At the bar end, objects have been successfully merged
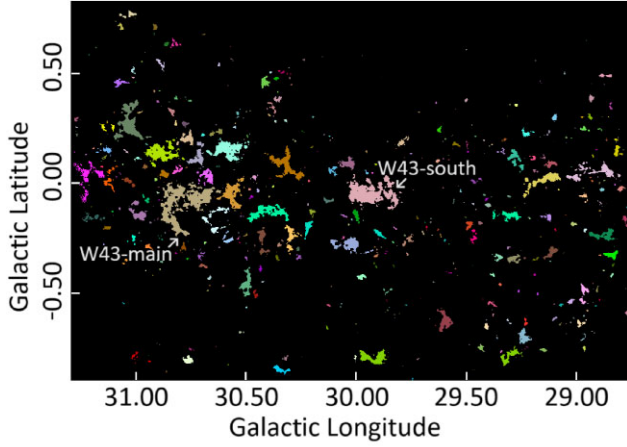
Figure A1. Merged catalogue at bar end at $\ell = 30°$ labelled with the location of W43.

Figure A2. Merged catalogue towards the galactic centre $\ell = 30°$.

together without regions being overmerged. We note that W43-main is missing a small section to the right, though W43-south has been successfully combined. Towards the galactic centre, however, we illustrate how the high column densities present and the crowding cause clouds to overmerge below $\ell = 2.5°$. As a result, we exclude $|\ell| = 2.5°$ from analysis.
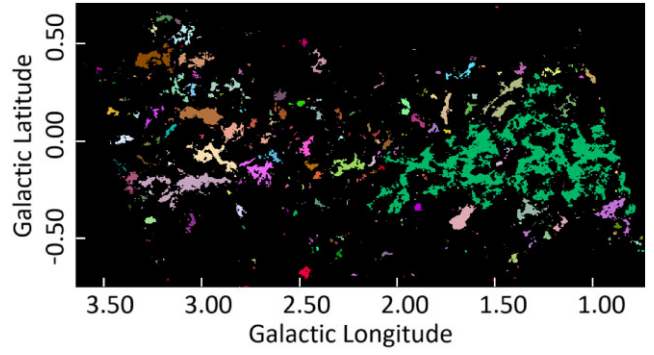
APPENDIX B: INVESTIGATING SOURCES OF BIAS THAT IMPACT THE PCA

We check if the bifurcation of cloud properties as a function of evolution could be caused by the cloud merging algorithm we use in Section 3.1. Potentially, the large clouds might preferentially contain clouds that merge, causing the mass increase that we see (a form of source crowding). To test this, we remade Fig. 12 but only include clouds that did not merge with another cloud. To help
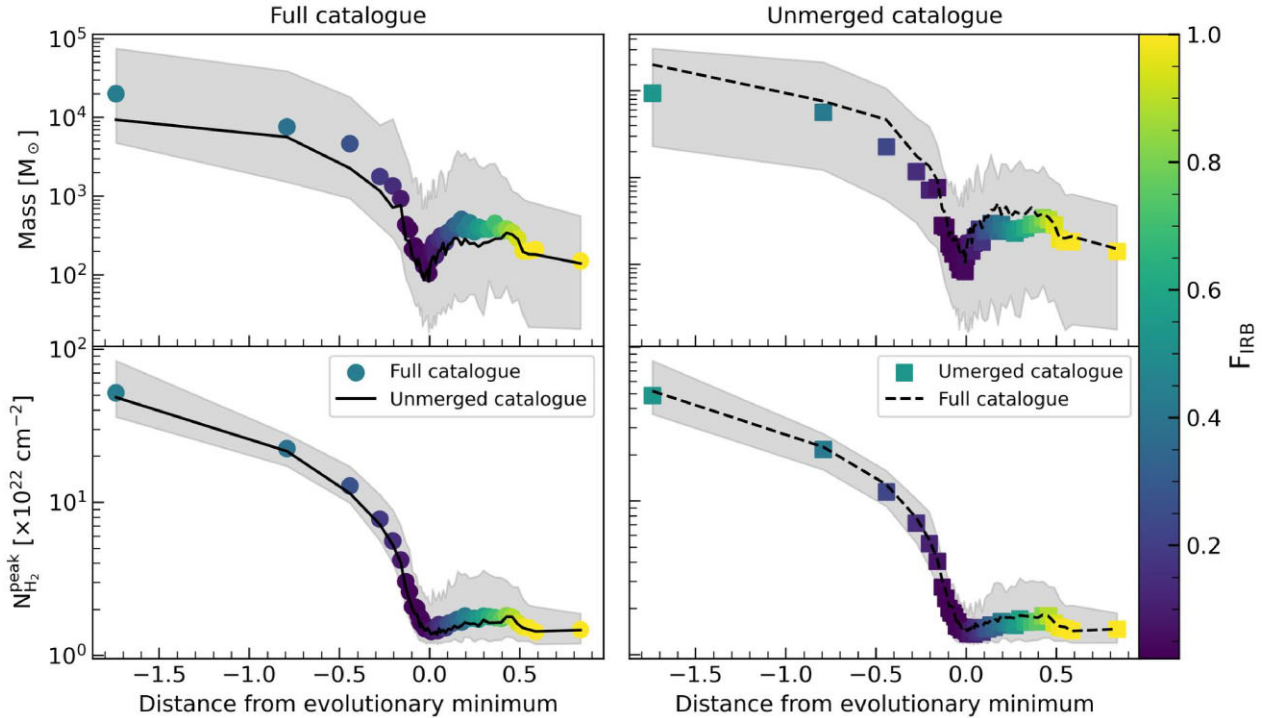

Figure A3. Median mass (top panels) and peak column density (bottom panels) as a function of their evolution. Left side (circle markers) shows the entire catalogue while the right side (square markers) shows a subsample of clouds that did not merge with another structure. The marker colours show the median f_{IRB} and the grey-shaded region show the 16–84 per cent sigma spread in the mass and peak column density. To aid comparison, solid black line of the left panel shows the values of the non-merged sample and the dash black line on the right panel shows the values of the entire catalogue.

with the comparison, we plot the full data set (left panel) and the non-merged data set (right panel) in Fig. A3. The black line on each panel show the values of the other panel to aid the comparison. We find that the median mass and the peak column density values are nearly identical for the merged and non-merged samples and we still see two evolutionary paths. Therefore, the cloud merging process does not cause there to be two cloud populations.

We next check if the potential distance bias (discussed in Section 4.2) is present in the PCA. Due to distance, we are more likely to find both higher mass clouds, and higher f_{IRB} fractions clouds as a function of distance (see Section 4.2 for explanation of f_{IRB} bias). Mass bias is a result of resolution. Clouds which are further away will have less detectable substructure and are more likely to blend neighbouring clouds into one object. Distance limiting the sample minimizes both f_{IRB} bias and mass bias, but removes most of the clouds on arm environments and limits our discussion. The distance bias can therefore affect the PCA, and therefore the azmuthial trends we find in the two cloud types. Using Kendall's τ correlation coefficient, we check for distance bias.

We find each component has a correlation coefficient of $\lesssim |0.1|$ with p-values of 0, except for PC3, which has a coefficient of 0.01 and p-value of 0.31 indicating the correlation is indistinguishable from random chance. We show their exact statistics in Table B1. For visual confirmation of these correlations we replot Fig. 11 on Fig. B1 and colour the markers using their distance to check if and how distance correlates with the components. We see there is no obvious correlation with distance. We also plot PC1 against distance on Fig. B2 and can see there a only a weak positive correlation. We are thus confident that distance does not play a dominant role in determining the PCA components, and since the PCA forms the majority of our analysis and discussion, we are also confident that distance bias is not responsible for the conclusions we draw.

We finally check how robust the PCA components are to incorrect distance assignments caused by the near-far ambiguity. In Section 3.2, we preferentially select near distances when multiple combined structures had matching velocities with both near and far assignments. Understandably, there will be incorrect assignments in our catalogue. Additionally, we find that the number of near-far assignments in the original Hi-GAL clump catalogue we use deviates from other clump based studies (such as Urquhart et al. 2018) by 20
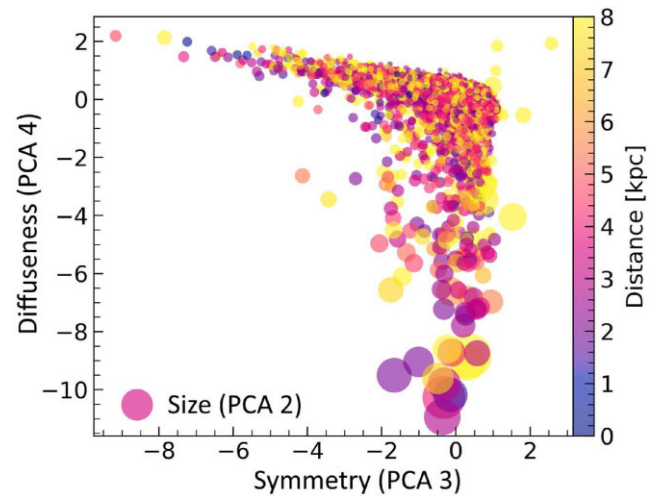

Figure B1. Score plot of the cloud catalogue using their principal components compared to their assigned distance. The diffuseness axis (PC4) is represented using the *y*-axis, the symmetry axis (PC3) is represented using the *x*-axis, the size of the markers shows the size of the clouds and the marker colours show the heliocentric distance assigned to each cloud.
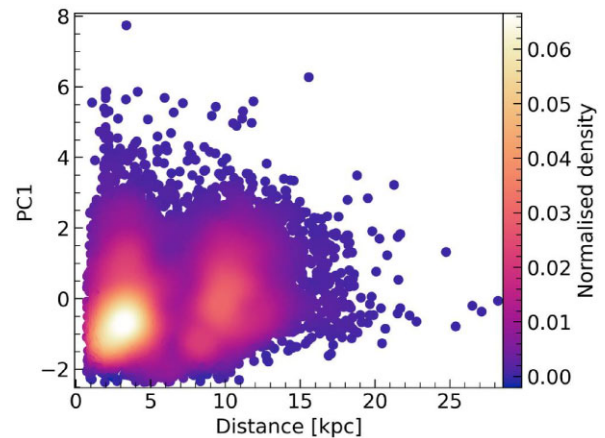

Figure B2. PC1 against assigned heliocentric distance. Colour of markers indicate the 2D histogram density of points.

per cent on the near-far assignment. To understand how sensitive our results are to incorrect assignments, we randomly swap 20 per cent of the distances to their near or far counterpart then recalculate the PCA 10 000 times. We then quantify the changes in the PCA by looking at statistics (i.e. mean) of how the eigenvectors and values change in Tables B2 and B3, respectively. We find there is very little spread and the average values are nearly identical to the original PCA vectors we

Table B1. Table showing how each principle component correlates with distance. We find weak or negligible correlation for each component.

	τ	p-Value
PC1 (evolution)	0.13	7.5×10^{-107}
PC2 (size)	-0.10	5.7×10^{-59}
PC3 (symmetry)	0.01	0.31
PC4 (diffuseness)	0.11	1.2×10^{-70}

Table B2. Statistics of how the normalized eigenvectors change after randomly swapping 20 per cent of the distances to their other distance solution 10 000 times and re-performing PCA.

	Peak column density	Mass	Temperature	f_{IRB}	Aspect ratio
Original value	0.301	0.092	0.679	0.661	-0.060
Median	0.303	0.093	0.678	0.660	-0.059
Mean	0.307	0.106	0.676	0.657	-0.058
Standard deviation	0.023	0.042	0.012	0.014	0.012
16th percentile	0.294	0.089	0.675	0.656	-0.070
84th percentile	0.313	0.123	0.680	0.663	-0.047

Table B3. Statistics of how the normalized eigenvalues change after randomly swapping 20 per cent of the distances to their other distance solution 10 000 times and re-performing PCA.

	PC1 (Evolution)	PC2 (Size)	PC3 (Symmetry)	PC4 (Diffuseness)	PC5
Original value	0.302	0.217	0.199	0.174	0.107
Median	0.302	0.218	0.200	0.173	0.107
Mean	0.303	0.219	0.199	0.172	0.107
Standard deviation	0.001	0.006	0.000(6)	0.007	0.000(7)
16th percentile	0.301	0.216	0.199	0.171	0.107
84th percentile	0.304	0.220	0.200	0.173	0.108
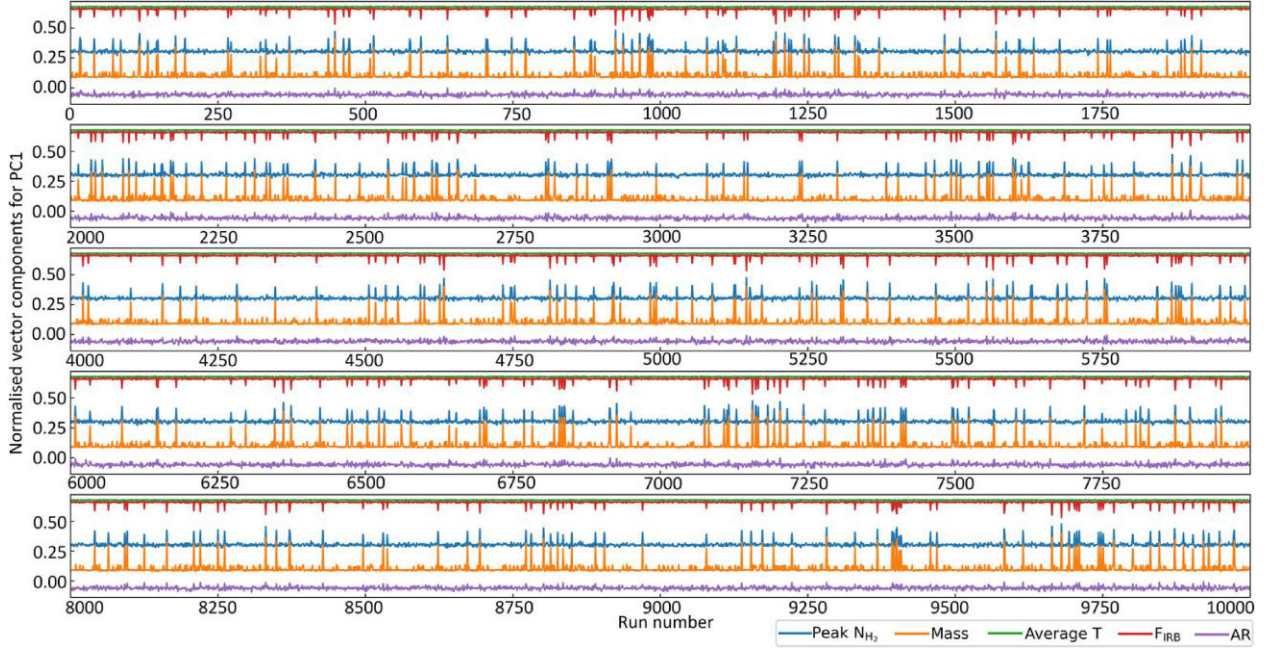
Figure B3. How the normalized eigenvectors change after randomly swapping 20 per cent of the distances to their other distance solution 10 000 times and re-performing PCA. Blue line shows the peak column density, orange shows the mass, green shows the average temperature, red shows $f_{\rm IRB}$, and purple shows the aspect ratio.

find, providing us confidence that our results and discussions are not impacted by incorrect near-far distance assignments. Furthermore, we find that the PCA solution changes slightly only 4 per cent of the time based of the variance between the data with the average values.

To illustrate these locations, we plot the values of the normalized eigenvectors and values for all 10 000 tests on Figs B3 and B4, respectively. The 'spikes' on the figures show where the changed distance assignment impacted the PCA solution.
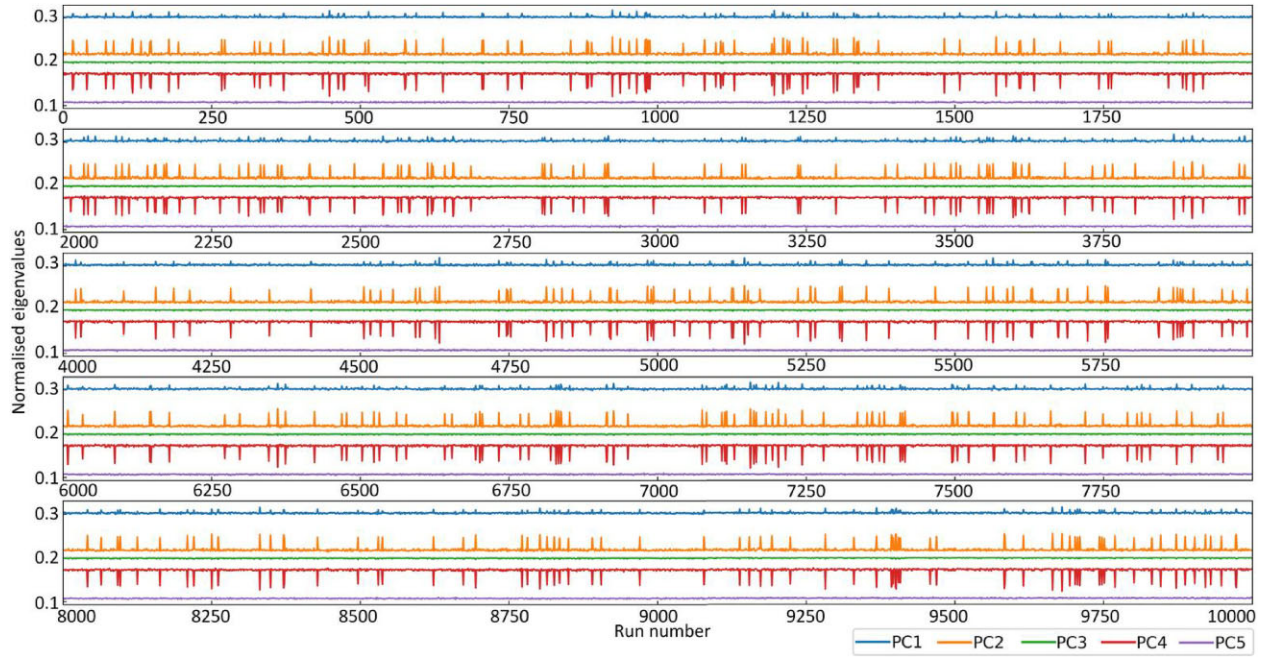
Figure B4. How the normalized eigenvalues change after randomly swapping 20 per cent of the distances to their other distance solution 10 000 times and re-performing PCA. Blue line shows PC1, orange shows PC2, green shows PC3, red shows PC4, and purple shows PC5.

APPENDIX C: FACE-DOWN MILKY WAY PLOTS

This section presents the top–down view of difference sub samples of the cloud catalogue over an illustration of the Milky Way structure.

We show the top–down view of the large and small cloud sample in Figs C1 and C2, respectively.
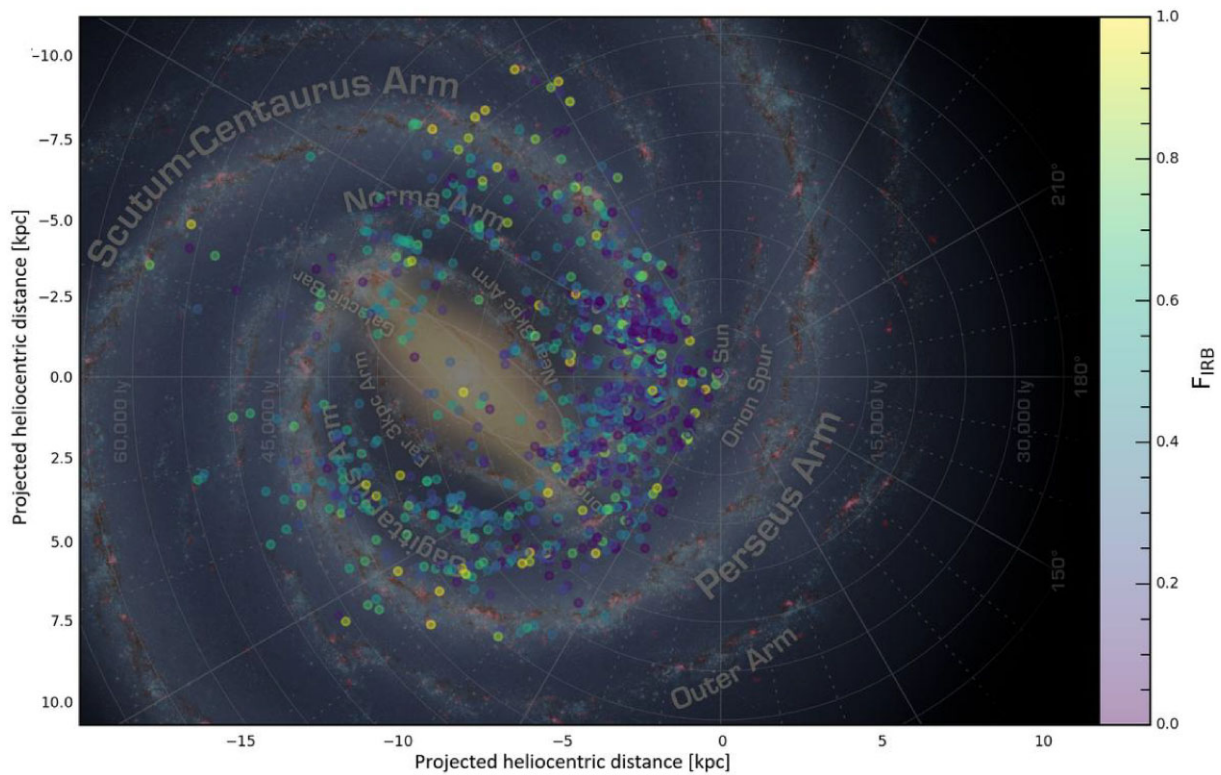
Figure C1. f_{IRB} of *large clouds* only overplotted over the Milky Way. Marker colours represent the f_{IRB} of each cloud shown.
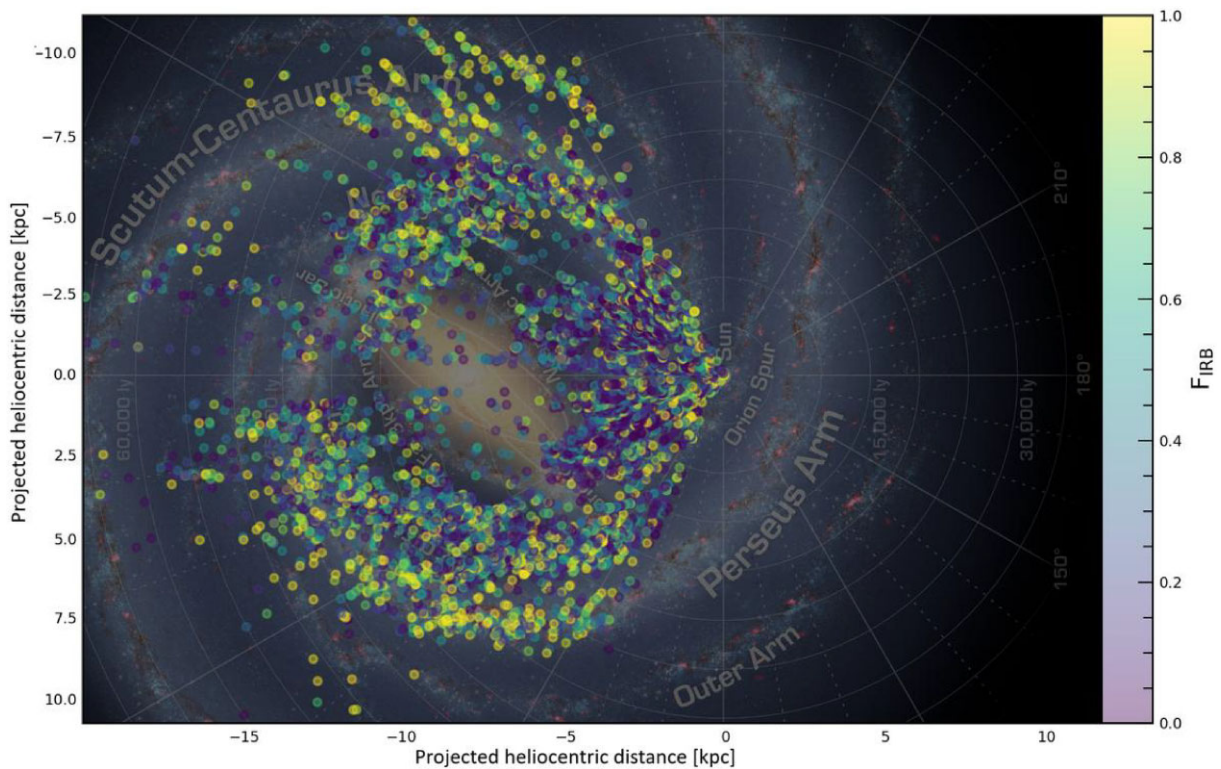

Figure C2. Same as Fig. C1 but for *small clouds* only.

This paper has been typeset from a TEX/LATEX file prepared by the author.